Wet and Dry Cold Surges over the Maritime Continent

Isaac Tan[1], Michael J. Reeder[1], Cathryn Birch[2], Simon Christopher Peatman[2], and Martin Simran Singh[1]

[1]Monash University
[2]University of Leeds

December 7, 2022

Abstract

Cold surges are synoptic weather systems that occur over the Maritime Continent during the boreal winter. They are characterised by the strengthening of prevailing low-level northerly to north-easterly winds, temperature falls of a few degrees over several days, and in some cases, extreme prolonged rainfall and flooding. We investigate the synoptic structure and development of cold surges through composites of dry, moderate and wet surges. Each surge category is defined by the distribution of precipitation averaged within a specified domain over the equatorial South China Sea.

Over the Maritime Continent, most of the dry (wet) surges occur during the suppressed (active) phases of the Madden-Julian Oscillation (MJO). Dry surges are characterised by cross-equatorial flow and positive mean sea-level pressure anomalies which reach the Southern Hemisphere, and enhanced descent or weaker ascent. Wet surges coincide with a cyclonic circulation over Borneo, a lack of cross-equatorial flow, and enhanced moisture and ascent. We find that diurnal precipitation patterns are consistent with convective onset being controlled by the mid-tropospheric buoyancy of an idealised entraining plume. This buoyancy diagnostic suggests that wet surges are characterised by a moister free troposphere because this reduces the effect of entrainment and allows convection to penetrate the lower troposphere.

Finally, deep (shallow) and relatively strong (weak) westerlies are found over southern Java and northern Australia during the dry (wet) surges. Consequently, Australian summer monsoon bursts are more likely to occur following dry cold surges. The westerlies are also explained as part of the larger-scale MJO circulations.

1   # Wet and Dry Cold Surges over the Maritime Continent

2   **I. Tan[1], M. J. Reeder[1,2], M. S. Singh[1,2], C. E. Birch[3], and S. C. Peatman[3]**

3   [1] School of Earth, Atmosphere and Environment, Monash University, Clayton, Victoria,

4   Australia

5   [2] Australian Research Council Centre for Climate Extremes, Australia

6   [3] Institute of Climate and Atmospheric Science, School of Earth and Environment, University of

7   Leeds, Leeds, United Kingdom

8   Corresponding author: Isaac Tan (isaac.tan@monash.edu)

9   **Key Points:**

10   - The synoptic structure and development of dry, moderate, and wet cold surge composites
11   over the Maritime Continent are investigated.

12   - Wet cold surges are characterised by a moister free troposphere that allows convection to
13   penetrate the lower troposphere.

14   - Australian summer monsoon bursts are more likely to follow dry cold surges, and are
15   primarily influenced by the Madden Julian Oscillation.

16 **Abstract**

17   Cold surges are synoptic weather systems that occur over the Maritime Continent during

18 the boreal winter. They are characterised by the strengthening of prevailing low-level northerly to

19 north-easterly winds, temperature falls of a few degrees over several days, and in some cases,

20 extreme prolonged rainfall and flooding. We investigate the synoptic structure and development

21 of cold surges through composites of dry, moderate and wet surges. Each surge category is defined

22 by the distribution of precipitation averaged within a specified domain over the equatorial South

23 China Sea.

24   Over the Maritime Continent, most of the dry (wet) surges occur during the suppressed

25 (active) phases of the Madden-Julian Oscillation (MJO). Dry surges are characterised by cross-

26 equatorial flow and positive mean sea-level pressure anomalies which reach the Southern

27 Hemisphere, and enhanced descent or weaker ascent. Wet surges coincide with a cyclonic

28 circulation over Borneo, a lack of cross-equatorial flow, and enhanced moisture and ascent. We

29 find that diurnal precipitation patterns are consistent with convective onset being controlled by the

30 mid-tropospheric buoyancy of an idealised entraining plume. This buoyancy diagnostic suggests

31 that wet surges are characterised by a moister free troposphere because this reduces the effect of

32 entrainment and allows convection to penetrate the lower troposphere.

33   Finally, deep (shallow) and relatively strong (weak) westerlies are found over southern

34 Java and northern Australia during the dry (wet) surges. Consequently, Australian summer

35 monsoon bursts are more likely to occur following dry cold surges. The westerlies are also

36 explained as part of the larger-scale MJO circulations.

37 **Plain Language Summary**

38   Cold surges are large-scale monsoon weather systems that bring enhanced north-easterly winds,

39   colder temperatures, and often extreme rainfall and flooding over the Maritime Continent region

40   between November and March each year. We investigate the structure and development of dry,

41   moderate, and wet cold surges. The three categories are defined based on rainfall averages over a

42   domain located near the equator, and are largely influenced by the Madden-Julian Oscillation

43   (MJO), which is the major fluctuation in tropical weather on weekly to monthly timescales. Of the

44   three categories, we find that dry surges are characterized by the highest pressure, and north-

45   easterly winds from the surge cross the equator into the Southern Hemisphere, which then turn to

46   become westerly. As a result, relatively strong westerly winds are found over southern Java and

47   northern Australia during dry surges, leading to bursts in the Australian summer monsoon. In

48   contrast, wet surges coincide with a cyclonic circulation over Borneo and increased moisture and

49   convection, and there are a lack of westerly winds over southern Java and northern Australia.

50   **1 Introduction**

51   Cold surges are synoptic weather systems that occur over the Maritime Continent during

52   the boreal winter (November-March; NDJFM), and are characterised by the strengthening of

53   prevailing low-level northerly to north-easterly winds, temperature falls of a few degrees over

54   several days, and in some cases, extreme prolonged rainfall and flooding (e.g. Ramage 1971;

55   Chang et al., 1979; Ding, 1994; Chang et al., 2004; Chang et al., 2005, Johnson and Chang 2007;

56   Wu et al 2007; Tangang et al., 2008; Fong and Ng, 2012; Pullen et al., 2015; Lim et al., 2017;

57   Xavier et al., 2020; MSS, 2022). They often produce bursts of convection around the equator,

58   affecting the coastal regions of South East Asia such as Vietnam, the Malaysian Peninsula, and

59   Singapore. These regions are located within the western half of the Maritime Continent, which is

60   the largest archipelago on Earth and a region of intense convection (e.g., Ramage, 1968; Neale and

61   Slingo, 2003; Argüeso et al., 2020).

62   Examples of extreme rainfall from cold surges are documented in Fong and Ng (2012),

63   including one on 9-10 December 1969 where torrential rainfall over the east coast of the Malaysian

64   Peninsula was observed, and a daily rainfall total of 483.1 mm was recorded at Singapore's climate

65   station. During another cold surge on 2 December 1978, a record high daily rainfall total of 512.4

66   mm was observed, which is about 25% of Singapore's annual average rainfall (Fong and Ng,

67   2012). The extreme rainfall from this surge resulted in seven deaths and the evacuation of hundreds

68   due to widespread flooding over the island. More recently, two strong cold surges that affected

69   Singapore and the surrounding region between 1–2 January and 8–13 January 2021 each had peak

70   daily rainfall amounts exceeding 200 mm at Singapore's climate station. These consecutive cold

71   surges were the primary contributors of the second wettest January in 152 years of record (MSS,

72   2022a).

73   Cold surges are driven by the strengthening of a large anticyclone over Siberia that

74   dominates the low-level circulation over Asia, often referred to as the "Siberian high" (e.g., Lim

75   and Chang, 1981; Lau and Li, 1984; Yihui, 1994; Fong and Ng, 2012). Southward intrusions of

76   the Siberian high often result in sudden surges of strong northerly to north-easterly winds that

77   propagate towards China and the South China Sea. As cold and dry winds strengthen equatorward

78   with the passage of the surge, their air temperature and humidity increase, and is associated with

79   warmer equatorial sea surface temperatures (Chang et al., 1979, 1983). In response to the

80   strengthening low-level winds, a cyclonic circulation often forms off the northwest coast of

81   Borneo, which is known as the Borneo vortex and is associated with enhanced deep convection

82   (e.g., Chang et al., 1979; Johnson and Houze, 1987; Chang et al., 2003; Chang et al., 2005).

83   From November to January, heavy rainfall from cold surges often affects Vietnam, the

84   Malaysian Peninsula, and Singapore (Fong and Ng, 2012; MSS, 2022a). Between February and

85   March, cold surges cross the equator about 75% of the time, resulting in drier conditions over the

86   entire Malaysian Peninsula, eastern Vietnam, and Sumatra, but enhanced rainfall over the Java Sea

87   and northwest of Australia (Xavier et al., 2020). It is also thought that cross-equatorial surges

88   sometimes trigger the onset of the Australian summer monsoon (e.g., Davidson et al., 1983; Love,

89   1985; Suppiah and Wu, 1998). The relative importance of cross-equatorial surges to the onset of,

90   and bursts in, the Australian summer monsoon compared to other influences such as midlatitude

91   fronts and the Madden-Julian Oscillation (MJO; e.g., Berry and Reeder, 2016; Narsey et al., 2017;

92   Narsey et al., 2018) have not yet been investigated.

93   Yang et al. (2019) examined the conditions for both wet and dry cold surges over Singapore

94   during NDJFM 1979-80 to 2017-18. They found that wet cold surges are characterised by a

95   strengthening of the moisture flux in the South China Sea, positive moisture flux convergence

96   anomalies between 0°N and 10°N two days before surge onset, and heavy rainfall over Singapore

97   on the day of onset. In contrast, dry surges exhibit negative moisture flux anomalies from 0°N–

98   15°N and positive anomalies from 0°S–12°S up to 5 days prior to the surge. Consistent with cross-

99   equatorial surges, these dry surges mostly occur later in the boreal winter season between January

100   and February.

101   Cold surges lasting 6 or more days that reach the low latitudes and exhibit distinct

102   precipitation signatures over the Maritime Continent region were classified into 4 types by

103   Abdillah et al. (2021). Of the four surge types, two are relevant to the equatorial Maritime

104   Continent region, namely the 'South China Sea type' and 'Both type'. The former mostly occurs

105   in the early winter months and is often associated with low-pressure vortices near Borneo leading

106   to heavy rainfall or flooding over South East Asia, whereas the latter is a combination of surges

107   that affect both the South China Sea and the Philippines Sea, and is characterised by the strong

108   southward propagation of both northerly wind and high-pressure anomalies that cross the equator.

109   These surges are also characterised by strong positive precipitation anomalies over the South China

110   Sea, western Maritime Continent, and Java.

111   According to Chang et al. (2005), the MJO modulates the frequency of cold surges and

112   contributes to variability in deep convection. The impact of deep convection is also affected by the

113   Borneo vortex, and its interaction with cold surges and the MJO. Chang et al. (2005) find that cold

114   surges enhance the contrast of enhanced (suppressed) deep convection over the South China Sea

115   when the Borneo vortex is present (absent). Cold surges strengthen the vortex and shift the vortex

116   centre from being located over the South China Sea to the western coast of Borneo. The strong

117   cyclonic horizontal shear over Borneo associated with enhanced equatorial westerly winds is also

118   present when the active convection portion of the MJO (i.e., phase 3 out of 4 based on Fig. 10 of

119   the study) is moving eastward of the Maritime Continent (Chang et al., 2005). Thus, the MJO may

120   inhibit weak cold surges since its circulation pattern directly opposes the north-easterly cold-surge

121   winds. Additionally, the vortex is least likely to be present when the inactive convective portion

122   of the MJO (i.e., phase 1 out of 4 based on Fig. 10 of the study) is over the Maritime Continent

123   (Chang et al., 2005). Therefore, the frequency of cold surges and vortex days is reduced during

124   periods when the MJO is present, and the overall relationship among the MJO, cold surges, and

125   the Borneo vortex are complex.

126   Lim et al. (2017) also studied the impacts and interactions of cold surges and the MJO on

127   rainfall over Southeast Asia. They found that the active phases of the MJO create a more

128   favourable environment for convection by moistening the atmosphere, which in turn enhances

129   conditional instability. Although less frequent, cold surges that occur during the active phases of

130   the MJO result in higher rainfall, and the most extreme rainfall events reported by Lim et al. (2017)

131   occurred during these conditions. Additionally, Xavier et al. (2020) show that cross-equatorial

132   surges in February and March, which are characterised by prolonged periods of strong meridional

133   flow at the equator, tend to reverse the MJO wind fields and hence suppress the rainfall anomalies

134   in the northern parts of the western Maritime Continent. Cold surge advection from the

135   midlatitudes can also act as a thermodynamic barrier for the convection to develop in the southern

136   parts of the South China Sea in the presence of strong cross-equatorial surges.

137   This paper describes the synoptic structure and development of cold surges over the

138   Maritime Continent using observational and reanalysis datasets. Additionally, we analyse the

139   thermodynamics of the convection associated with cold surges from the perspective of plume

140   buoyancy. Section 2 outlines the data and methodologies used. Section 3 investigates the

141   climatologies of the seasonal and diurnal cycles of non-surge days, and dry, moderate, and wet

142   surges. Section 4 contrasts and discusses the synoptic structure of dry, moderate, or wet cold surges

143   using long-term composites. Section 5 analyses the relationship between the MJO, cold surges and

144   bursts in the Australian summer monsoon. Conclusions follow in Section 6.

145   **2 Data and Methods**

146   *2.1 ERA5 and GPM*

147   Output from the fifth reanalysis of the European Centre for Medium-Range Weather

148   Forecasts (ECMWF ERA5; Hersbach et al., 2019) is used to composite long-term observations

149   over a 20-year climatological period from November 2000 to March 2020 (NDJFM 2000-01 to

150   2019-20). The ERA5 data have a horizontal grid spacing of 0.25° x 0.25° and we use 27 vertical

151   levels from 1000 to 100 hPa. Daily averages of hourly resolution data are computed for the

152   following ERA5 fields: mean sea level pressure (MSLP), total column water vapour (TCWV),

153   zonal and meridional winds, vertical motion (ω), temperature, and specific humidity. The

154   temperature and specific humidity are also computed at 3-hourly intervals.

155   We use Global Precipitation Measurement (GPM; Huffman et al., 2019; National

156   Aeronautics and Space Administration [NASA], 2021) data to analyse the precipitation over the

157   same 20-year period. It has a horizontal grid spacing of 0.1° x 0.1° and the multi-satellite

158   precipitation estimate with gauge calibration field (i.e., 'precipitationCal') is used (Huffman et al.,

159   2019). The dataset containing the final estimate of daily accumulated GPM precipitation (i.e.,

160   GPM IMERG Final Precipitation L3) is used for the daily mean composites, and 30-minute

161   resolution data is used to analyse the diurnal cycle at 3-hourly intervals.

162   Finally, we use daily data for the MJO index over the entire climatological period, where

163   the real-time multivariate MJO index (RMM; Wheeler and Hendon., 2004) is used to identify the

164   amplitudes and phases of the MJO.

165   *2.2 Cold surge identification*

166   We identify cold surges by applying various criteria from Chang et al. (2005) and Lim et

167   al. (2017), as specified in Table 1.

168

169   *Table 1: Cold surge definition and criteria used in this study.*

Variable	Condition
Mean sea level pressure (MSLP)	Exceed 1020 hPa anywhere within 18-22°N, 105-122°E (brown box in Figure 1).
925 hPa wind speed	At least 0.75 standard deviations above the 20-year NDJFM mean when averaged over 5-10°N, 107-115°E (magenta box in Figure 1).
925 hPa wind direction	Between 337.5° (north-north-westerly) and 90° (easterly).

170   Based on the ERA5 climatology for NDJFM 2000-01 to 2019-20, the wind speed must be at least

171   approximately 11.5 m s^{-1} to satisfy the wind speed threshold. The cold surges must also satisfy the

172   criteria for at least two consecutive days (Yihui, 1990). The advantage of using this cold surge

173   identification method is that it eliminates weather systems with easterly flow from the Philippines,

174   such as typhoons (Xavier et al., 2020). From these constraints in the wind speed and direction,

175   only the 'South China Sea type' and 'Both type' of cold surge from Abdillah et al. (2021) are

176   identified. These are also the only surge classifications that affect the Maritime Continent region.

177   In total, the requirement for two consequtive surge days eliminates 40 single-day surges within the

178   20-year climatological period, leaving a total of 545 cold surge days and 132 surges that are two

179   days or longer in duration.

180   *2.3 Wet vs. dry cold surges*

181   Precipitation quartiles are used to distinguish between dry (below the lower quartile – 33

182   surges; 114 days), wet (above the upper quartile – 33 surges; 124 days), and moderate (between

183   the quartiles – 66 surges; 307 days) cold surges for NDJFM 2000-01 to 2019-20. The precipitation

184   thresholds for each category are based on precipitation averages over a domain encompassing

185   Singapore and parts of Malaysia, Sumatra, and Borneo (see the "Precipitation domain", blue box

186   in Figure 1). The boundary for the lower quartile is approximately 3.5 mm d^{-1} and for the upper

187   quartile it is approximately 17.4 mm d^{-1}. Anomalies for each variable are calculated by subtracting

188   the 31-day centred moving average seasonal cycle climatology. Composites over the 20-year

189   climatology are used to analyse the synoptic-scale structure and development of cold surges, and

190   the environments that characterise the dry, moderate, or wet surges. Lagged composites are

191   computed between day -5 and day +5 relative to the surge onset for each cold surge category.

192   Composite maps are plotted within 15°S–25°N, 95°E–125°E (see the dashed red box in Figure 1)

193   and 5°S-20°S, 95°E-150°E for the Australian summer monsoon analysis (encompasses the

194   "Australian monsoon domain", green box in Figure 1).
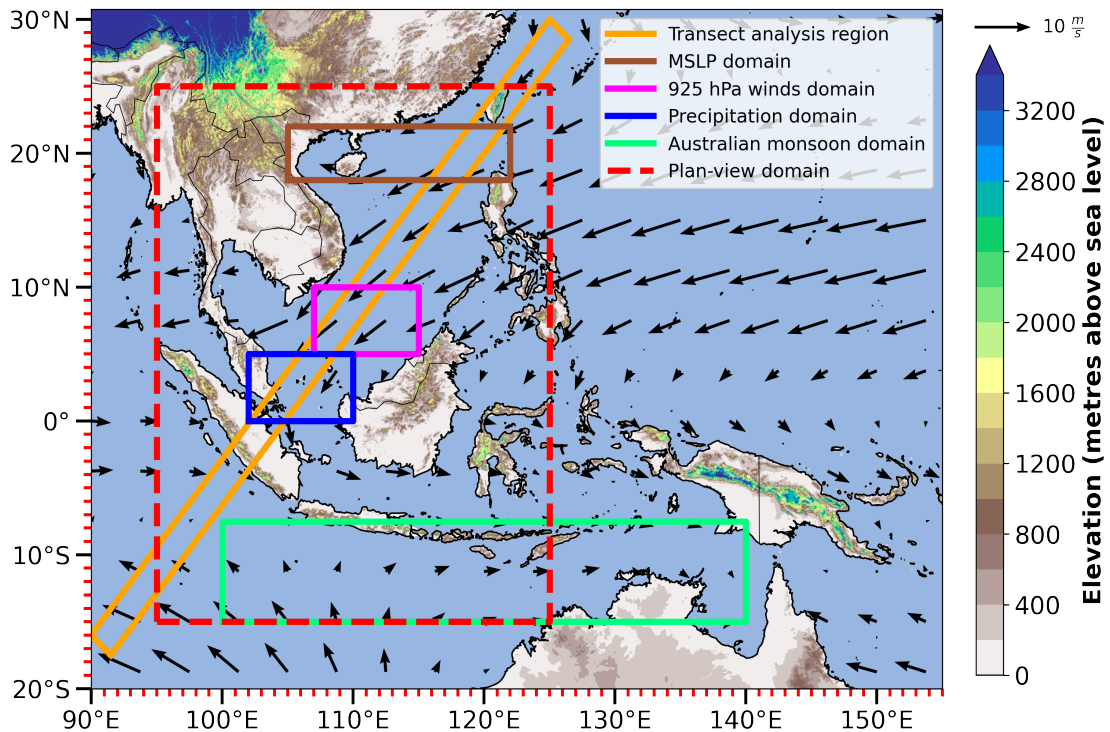
Figure 1: Map of the Maritime Continent region that depicts the transect analysis region (orange box), the cold surge indices domains for MSLP (brown box) and 925 hPa winds (magenta box), the precipitation domain to contrast wet and dry cold surges (blue box), the composite maps analysis region (dashed red box), and the Australian monsoon domain (green box). 925 hPa wind vectors for the NDJFM 2000-01 to 2019-20 mean climatology.

195   The relationship between cold surge days in each category and the MJO is also analysed.

196   First, the RMM index (Wheeler & Hendon, 2004) is used to categorise days by phase of the MJO.

197   Days with RMM amplitude greater than 1 are considered to be in one of phases 1 to 8 as defined

198   by the RMM index, otherwise the days are considered to be non-MJO days. For each surge type,

199   we then calculate the normalised frequency of days in each phase of the MJO. This is defined as

200   the fraction of days of a particular surge category that are in a particular phase of the MJO divided

201   by the fraction of all days in the climatology that are in the same phase of the MJO. For the

202   Maritime Continent, phases 2-4 are considered MJO active phases, while phases 5-7 are considered

203   MJO inactive phases.

204   *2.4 Plume buoyancy (B_L)*

205   We also analyse the thermodynamics of the convection associated with cold surges using

206   a diagnostic for the mid-tropospheric buoyancy experienced by an idealised entraining plume,

207   which we denote B_L. Similar diagnostics have been shown to closely relate to the onset of

208   convection over tropical regions in general (e.g., Gregory, 2001; de Rooy and Siebesma, 2010;

209   Ahmed and Neelin, 2018). Here we apply the formulation of Adames et al. (2021), in which B_L is

210   defined:

211
$$B_L = \frac{g}{\kappa_L}\left(W_B \frac{\theta_{eB} - \theta_{eL}^*}{\theta_{eL}^*} - W_L \frac{\theta_{eL}^* - \theta_{eL}}{\theta_{eL}^*}\right) \qquad \text{(Eq. 1)}$$

212   where
$$\kappa_L = 1 + \frac{L^2 q^*}{c_p R_v T^2} \text{ ,} \qquad \text{(Eq. 2)}$$

213
$$W_B = \frac{\Delta P_B}{\Delta P_L} ln(1 + \frac{\Delta P_L}{\Delta P_B}) \text{ ,} \qquad \text{(Eq. 3)}$$

214   and
$$W_L = 1 - W_B \qquad \text{(Eq. 4)}$$

215   In Eq. 1, $g = 9.8$ m s^{-2}, θ_{eB} and θ_{eL} denote the equivalent potential temperatures within the deep

216   boundary layer (DBL; 1000 to 850 hPa) and lower free troposphere (LFT; 850 to 600 hPa)

217   respectively, and θ_{eL}^* is the saturation equivalent potential temperature within the LFT. In Eq. 2,

218   κ_L is the scaling term, where $L = 2.5$ x 10^6 J kg^{-1} K^{-1} is the latent heat of vaporisation, $c_p = 1004$ J

219   kg^{-1} K^{-1} is the specific capacity of dry air, $R_v = 461$ J kg^{-1} K^{-1} is the gas constant of water vapour,

220   q^* is the saturation specific humidity, and T is the temperature. In Eq. 3 and 4, ΔP_B and ΔP_L denote

221   the pressure thickness of the DBL and LFT (150 and 250 hPa) respectively.

222   While buoyancy is defined using temperature or potential temperature (θ), B_L is defined in

223   terms of equivalent potential temperature (θ_e) because it is approximately conserved during moist

224   adiabatic processes. Adames et al. (2021) nevertheless interpret B_L as a measure of the buoyancy

225   of an air parcel as it rises to the top of the LFT layer, mixing with its environment. We may

226   therefore see B_L as a measure of convective instability of the lower troposphere that accounts for

227   the effects of mixing. In particular, we note that there are two terms in Eq. 1, each given a weighting

228   W_B or W_L. The first term is the 'undilute B_L', which is a traditional measure of the convective

229   instability of the lower troposphere (Raymond et al., 2015; Adames et al., 2021). For this measure

230   of convective instability, the parcel is assumed not to mix as it passes through the LFT. Positive

231   values of undilute B_L indicate unstable profiles with a high potential for convection, provided air

232   is lifted from the boundary layer (i.e., the DBL at 850 hPa) without mixing with its environment.

233   The second term is a function of the saturation deficit of the LFT, and it represents the reduction

234   in buoyancy in a rising plume as it entrains and is diluted by free-tropospheric air. The importance

235   of the second term is set by the weights W_B and W_L, which describe the relative mass inflow to the

236   plume from the DBL and LFT. For the parameters used here (taken from Adames et al. 2021), W_B

237    $= 0.59$ and $W_L = 0.41$.

238   As B_L increases from negative values towards zero, Adames et al. (2021) show that

239   precipitation increases exponentially (see their Fig. 3). They also note a critical value of $B_L \sim -0.02$

240   m s^{-2} that marks the beginning of the transition to a linear precipitation regime, where precipitation

241   increases linearly and rapidly with increasing values of B_L. Although B_L is averaged between 15°N

242   and 15°S in the Adames et al. (2021) study, here we compute B_L over the precipitation domain and

243   the composite maps analysis region (see the blue and dashed red boxes respectively in Figure 1).

244   **3 Climatologies of the Seasonal and Diurnal Cycles**

245   *3.1 Seasonal cycle of wet and dry cold surges*

246   There is a clear seasonal cycle in GPM precipitation, which is averaged over the

247   precipitation domain and during NDJFM. The 31-day centred moving average precipitation peaks

248   at approximately 11.5 mm d^{-1} in the middle of December, and is lowest at approximately 4.1 mm

249   d^{-1} in early March (Figure 2a). Most wet surge days are also found in December and January (57

250   and 42 days respectively) and most dry surge days are found in January and February (39 and 54

251   days respectively; Figure 2b).

252   Overall, cold surge days contribute approximately 30% of total rainfall within the 20-year

253   climatological period (545 surge days out of 3025 days, or approximately 18%), where close to

254   half of the surge rainfall contribution occurs in each of the wet and moderate surge days

255   (approximately 14.7% and 14.3% respectively), and less than 1% in the dry surge days (Figure

256   2c). The higher contribution of rainfall from cold surges relative to the fraction of cold surge days

257   within the 20-year period is explained by the overall higher daily mean rainfall rate during cold

258   surge days (approximately 12.3 mm d^{-1} for all cold surge days and 10.5 mm d^{-1} for moderate

259   surges) than non-surge days (approximately 6.4 mm d^{-1}; Figure 2d). Dry and wet surges also have

260   a daily mean rainfall rate of approximately 1.7 mm d^{-1} and 26.6 mm d^{-1} respectively. When the

261   seasonal cycle is removed, there are individual days within the wet surge category that fall below

262   the climatological mean (20 out of 124 days) and vice versa for dry surges (7 out of 114 days).

263   This is expected since the precipitation quartiles for each surge category are based on the mean

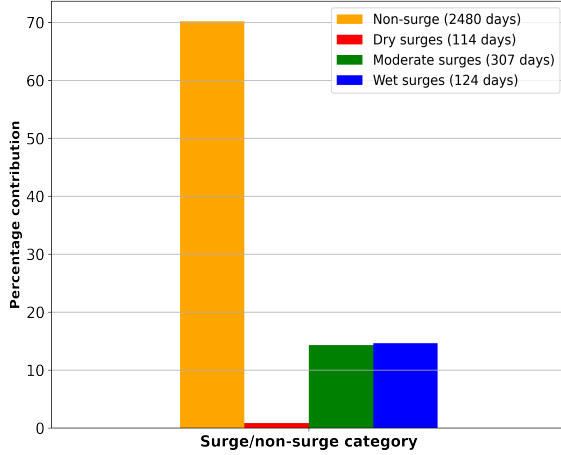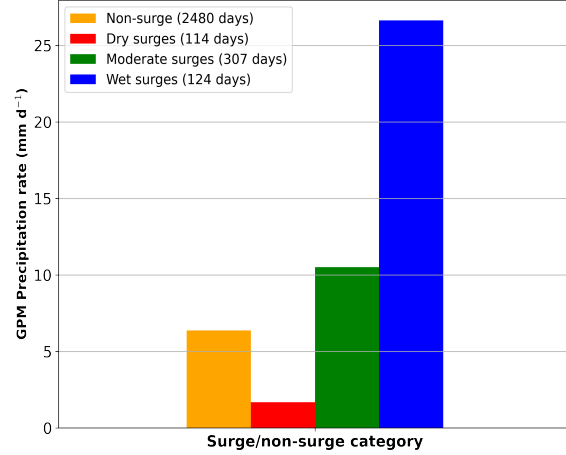264   precipitation of entire cold surges rather than individual cold surge days.
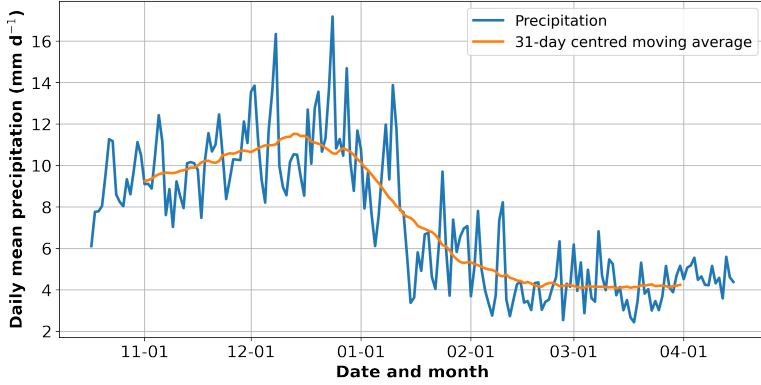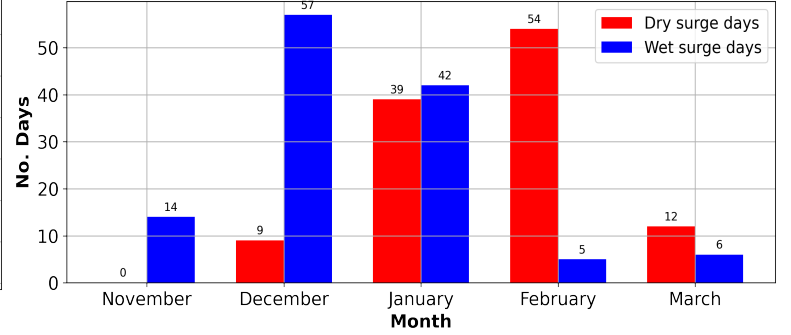
Figure 2: (a) Seasonal cycle of daily GPM precipitation from 1 November to 31 March (blue lines) with 31-day centred moving average curves (orange lines) averaged over 2000-01 to 2019-20. (b) Distribution of dry (red bars) and wet (blue bars) cold surge days by month over the NDJFM season. (c) GPM precipitation percentage contribution and (d) daily mean GPM precipitation rates. Non-surge days (orange), and dry (red), moderate (green), and wet (blue) cold surge days.

265   *3.2 Diurnal cycle of plume buoyancy and GPM precipitation*

266   There is a clear relationship between daily mean values of B_L and GPM precipitation

267   averaged over the precipitation domain on individual days within the 20-year period for non-surge

268   days and each of the three surge categories (Figure 3a). Most wet surge days (119 out of 124 days)

269   exceed the -0.02 m s^{-2} threshold for B_L while most dry surge days fall below the threshold (94 out

270   of 114 days). Overall, the cold surge days are closer to the threshold, but this may be simply due

271   to the smaller sample size (545 days) compared to non-surge days (2480 days).
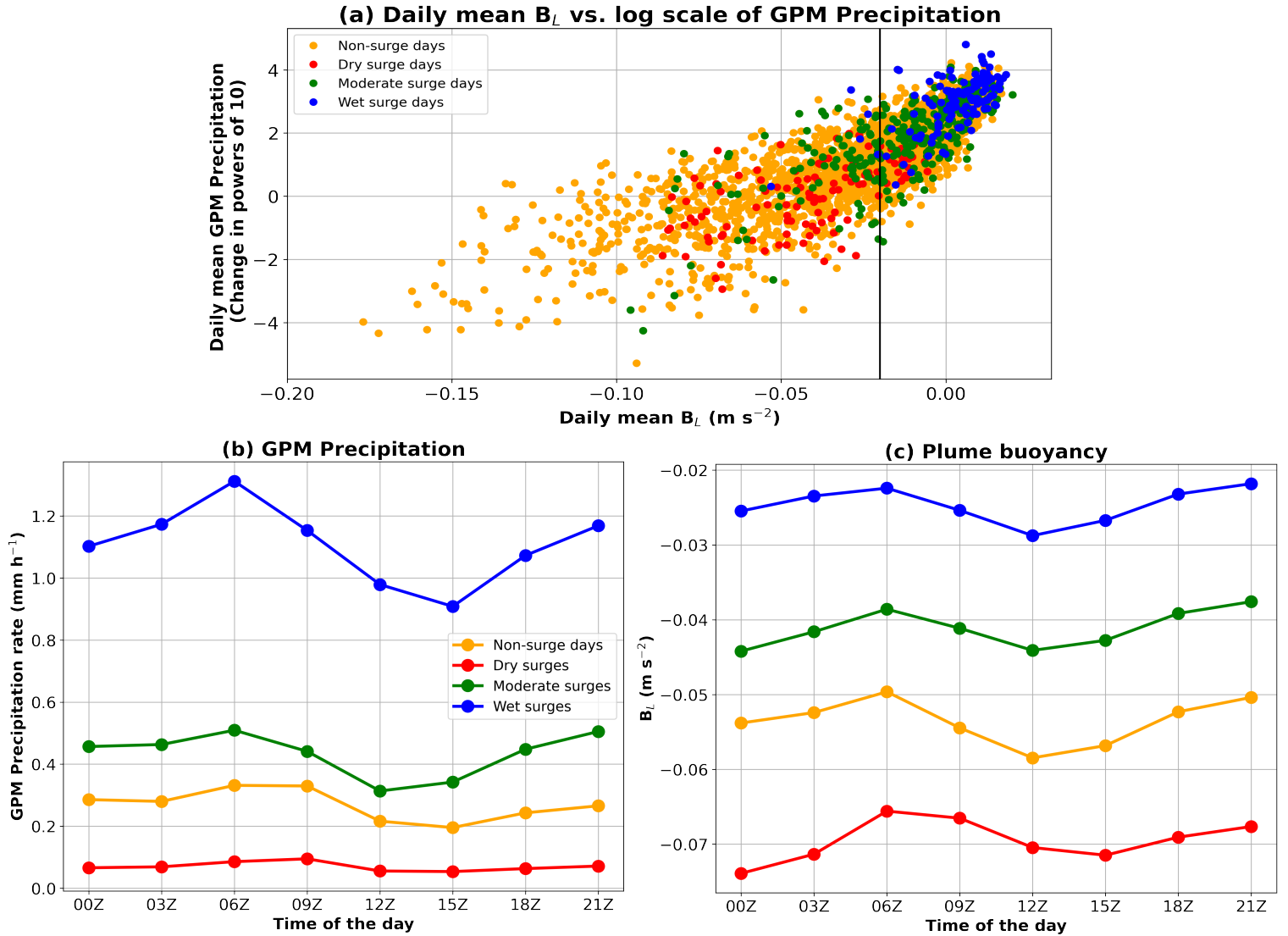
Figure 3: (a) Daily mean B_L vs. log scale of GPM precipitation over the precipitation domain in NDJFM 2000-01 to 2019-20. Non-surge days (orange), and dry (red), moderate (green), and wet (blue) cold surge days. The vertical black line is drawn at the -0.02 m s^{-2} threshold for B_L. Diurnal cycle of mean (b) GPM precipitation rate and (c) B_L. Non-surge days (orange), and dry (red), moderate (green), and wet (blue) cold surge composites.

272   In terms of the diurnal cycle, both the hourly precipitation rate (Figure 3b) and B_L (Figure

273   3c) over the precipitation domain are highest in the wet surge composites, followed by the

274   moderate, non-surge, and dry composites. In the wet and moderate surge composites, GPM

275   precipitation peaks at 06Z (14:00 LST; approximately 1.31 and 0.509 mm h^{-1} respectively) and the

276   diurnal contrasts are more pronounced. Precipitation rates at 21Z (05:00 LST) for the wet and dry

277   composites (approximately 1.17 and 0.505 mm h^{-1} respectively) are also well above the daily mean

278   values (approximately 1.11 and 0.44 mm h^{-1} respectively), and closer to the 06Z (14:00 LST) peak

279   compared to the non-surge and dry surge composites, which is most likely because of offshore

280   precipitation during the nocturnal hours. The precipitation rate peaks between 06Z and 09Z (14:00

281   LST and 17:00 LST) in the non-surge composites (approximately 0.33 mm h^{-1}), and 09Z (17:00

282   LST) in the dry surge composites (approximately 0.09 mm h^{-1}). On the other hand, troughs in the

283   diurnal cycle occur at 15Z (23:00 LST) for both the wet surge and non-surge composites

284   (approximately 0.91 and 0.20 mm h^{-1} respectively), between 12Z and 15Z (20:00 LST and 23:00

285   LST) in the dry (approximately 0.05 mm h^{-1}), and 12Z (20:00 LST) in the moderate surge

286   composites (approximately 0.31 mm h^{-1}). In contrast, there is a daytime peak of B_L at 06Z (14:00

287   LST) in all cases, and a greater peak at 21Z (05:00 LST) in the wet and moderate surge composites

288   (approximately -0.022 and -0.038 m s^{-2} respectively) since nocturnal convection occurs over the

289   ocean in these cases. Nocturnal troughs are observed at 12Z (20:00 LST) for all categories but 15Z

290   (23:00 LST) in the dry surge composites, and a lower minimum at 00Z (08:00 LST) for the dry

291   and moderate composites (approximately -0.074 and -0.044 m s^{-2} respectively).

292   Given the timings of peaks and troughs for both GPM precipitation and B_L in Figures 3b

293   and 3c, we compare their spatial distribution for the dry and wet surge composites by averaging

294   over 06Z and 09Z (14:00 LST and 17:00 LST) for the daytime average (Figures 4a, c, e, g), and

295   18Z and 21Z (02:00 LST and 05:00 LST for the nocturnal average (Figures 4b, d, f, h). The diurnal

296   cycles are compared on day +1 relative to surge onset, which is when the cold surge reaches its

297   peak over the precipitation domain and most of the South China Sea. In both the dry and wet surge

298   composites, wet anomalies are generally observed over land areas during the daytime average

299   (Figures 4a, c), and over the surrounding ocean during the nocturnal average (Figures 4b, d) due

300   to the offshore propagation of precipitation at night. The diurnal cycle of precipitation is strongest

301   over Sumatra, Java, and Sulawesi island. In the distribution of B_L (Figures 4e, f, g, h), the diurnal

302   cycle is clearest over Java, where areas which exceed the -0.02 m s^{-2} threshold are consistent with

303   areas of strongly enhanced (exceeding 1 mm h^{-1}) wet anomalies during the daytime average
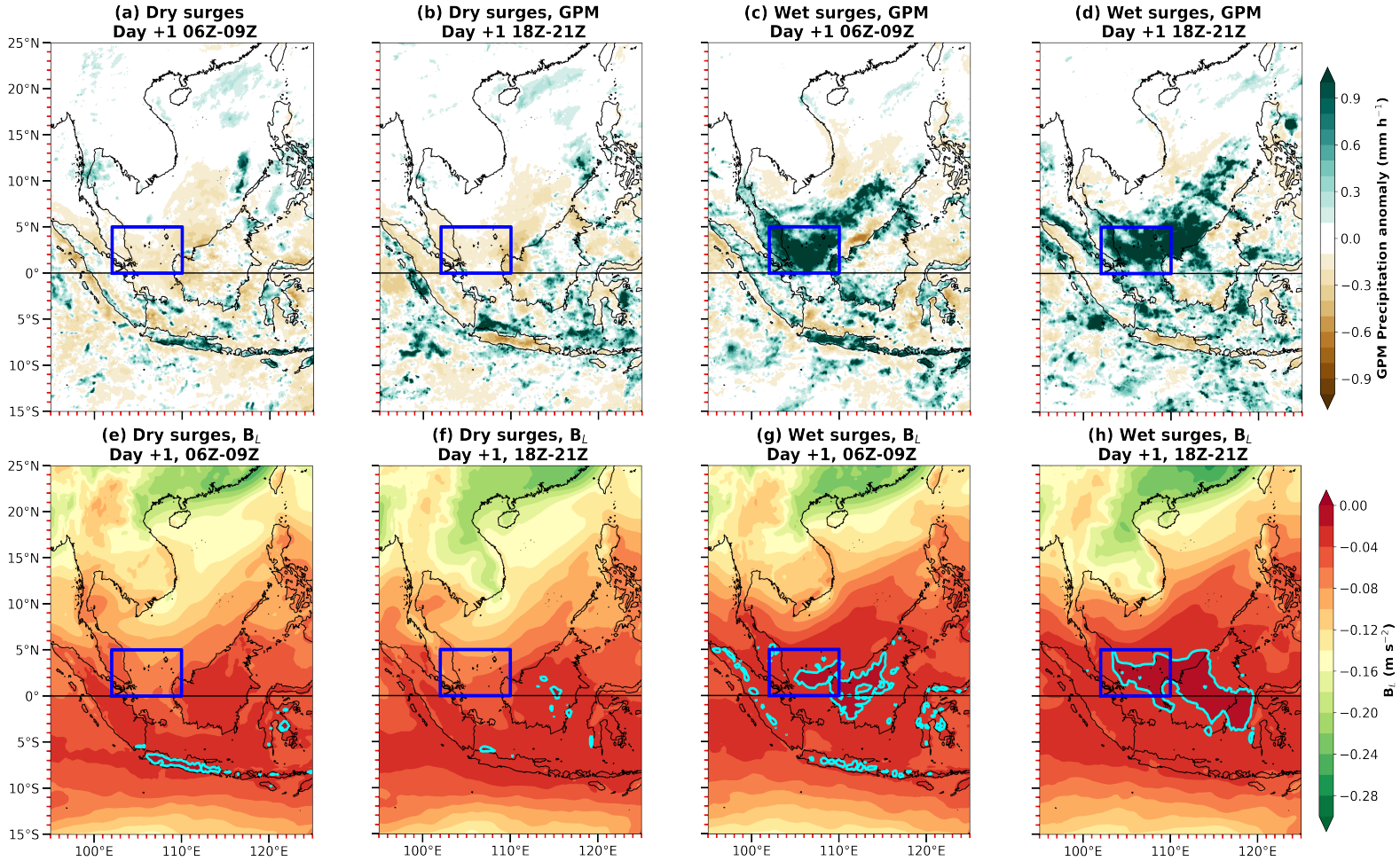
304   (Figures 4e, g).

Figure 4: Composite maps of (a-d) GPM precipitation anomalies with the seasonal cycle removed, and (e-h) layer average (850-600 hPa) values of B_L. Averages taken over 06Z and 09Z (a, c, e, g), and 18Z and 21Z (b, d, f, h). Dry and wet cold surges on day +1 relative to surge onset. The precipitation domain is depicted by the blue box. The cyan contours indicate the -0.02 m s^{-2} threshold for the B_L linear precipitation regime described in Adames et al. (2021).

305   Over the precipitation domain, the diurnal cycle is suppressed. Dry anomalies (-0.1 to -0.4

306   mm h^{-1}) are observed in the dry surge composites due to the propagation of colder and drier surge

307   air from the northern South China Sea. Strongly enhanced wet anomalies are observed over much

308   of the domain and equatorial South China Sea in the wet surge composites, regardless of the time

309   of day. For the wet composites, there is a land-ocean contrast along the north-west coast of Borneo

310   between the daytime and nocturnal average. The strongly enhanced wet anomalies are more

311   widespread during the nocturnal average over this region, which is consistent with the large area

312   where B_L exceeds the threshold value in Figure 4h.

313   Overall, B_L distinguishes the three classes of cold surges well, implying that wet surges are

314   characterised by a moister free troposphere, which allows convection to penetrate through the

315   lower troposphere. This implication will be further investigated in the lagged composite analysis

316   of TCWV and 700 hPa ω anomalies in the next section.

317   **4 Synoptic Structure of Cold Surges**

318   *4.1 The development of cold surges over the Maritime Continent*

319   In this section, we investigate the synoptic environments of each cold surge category using

320   lagged composite anomalies of TCWV (Figure 5), and ω at 700 hPa (not shown). The 925 hPa

321   wind anomaly vectors are also shown on each map.

322   The strength of the north-easterly surge wind anomalies is similar in the three surge

323   categories, although their characteristics near the equator differ in the day +1 maps. The dry surge

324   composites are characterised by cross-equatorial flow that reaches equatorward to Java, with

325   westerly anomalies around Java (Figure 5d). In contrast, the wet surge composites coincide with a

326   cyclonic circulation between Borneo and the Malaysian Peninsula instead of cross-equatorial flow

327   (Figure 5e). The moderate surge composites depict weaker cross-equatorial flow and westerly

328   anomalies over Java compared to the dry surge composites (Figure 5f).

329   Negative TCWV anomalies from the cold surge extend to the equator in the dry surge

330   composites (-1 to -5 mm), transitioning to weak positive anomalies around Java (+1 to +2 mm;

331   Figures 5a, d). These negative anomalies cover almost the entire precipitation domain and most of
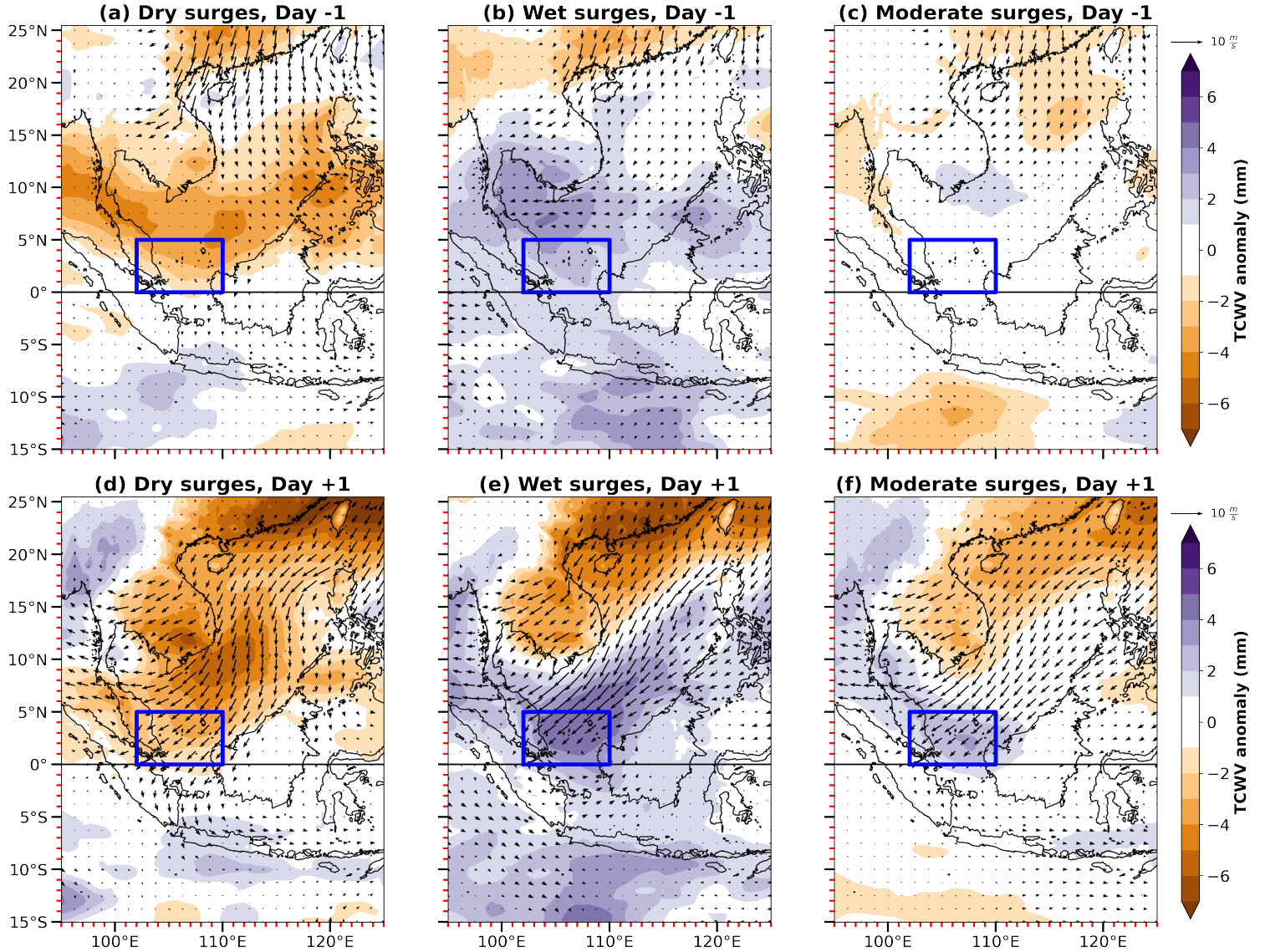
Figure 5: Lagged composite maps of daily mean TCWV anomalies with the seasonal cycle removed. Daily mean 925 hPa horizontal wind anomaly vectors. (a, d) Dry, (b, e) wet, and (c, f) moderate cold surges on day -1 (top row) and day +1 (bottom row) relative to surge onset. The precipitation domain is depicted by the blue box.

332   the South China Sea by day -1. The dry anomalies strengthen and peak under -7 mm to the

333   northeast of Taiwan on day +1 as the cold surge reaches its peak, while the strengthening cross-

334   equatorial flow coincides with the positive anomalies over Java. In the wet surge composites

335   (Figures 5b, e), widespread positive TCWV anomalies are already evident prior to surge onset (+2

336   to +4 mm). A meridional TCWV anomaly gradient is found on day +1, ranging from over +4 mm

337   over the equator to -6 mm over the northern South China Sea. This sharp gradient is consistent

338   with the convection near the equator in contrast to drier surge air over the northern South China

339   Sea. Weaker TCWV anomalies are observed in the moderate surge composites on day -1 over the

340   precipitation domain and much of the South China Sea (-2 to +1 mm; Figure 5c). On day +1 (Figure

341   5f), the anomalies follow a similar pattern to that of the wet surge composites, although the

342   meridional moisture gradient is weaker, ranging from +3 mm at the equator to -5 mm over the

343   northern South China Sea.

344   In each cold surge category, dry air from the surge is accompanied by positive 700 hPa ω

345   anomalies (i.e., stronger descent or weaker ascent relative to climatology), particularly on day +1.

346   Positive anomalies associated with the surge over Southern China are most widespread in the dry

347   surge composites (peaking close to 0.10 Pa s^{-1}), and weaker anomalies are observed over most of

348   the South China Sea (+0.00 to +0.03 Pa s^{-1}). These positive anomalies strengthen between day -1

349   and day +1, and negative anomalies strengthen around Java (-0.01 to -0.06 Pa s^{-1} over most parts).

350   It is likely that both the lack of moisture from negative TCWV anomalies and lack of ascent around

351   the equatorial South China Sea in the dry surge composites enable dry air to be advected towards

352   the equatorial latitudes. From day -1, areas of enhanced ascent are already evident over much of

353   the equatorial South China Sea in the wet surge composites (-0.01 to -0.06 Pa s^{-1}). Large areas of

354   strongly enhanced ascent develop and strengthen by day +1 (under -0.10 Pa s^{-1} over much of the

355   precipitation domain), which is consistent with GPM precipitation anomaly patterns from Figures

356   4c, d. In the moderate surge composites, the 700 hPa ω anomalies are relatively weak over the

357   precipitation domain on day -1 (-0.03 to +0.03 Pa s^{-1}). The anomaly patterns also follow a similar

358   structure to the wet surge composites from day +1, with enhanced ascent over the precipitation

359   domain (peaking close to -0.10 Pa s^{-1}).

360   Cold surges over the northern South China Sea are characterised by below average

361   moisture, and enhanced descent. In the dry surge composites, the stronger descent or weaker

362   ascent, and dry air reach the precipitation domain, whereas relatively moist air ascent and enhanced

363   ascent is found over the Java area. Enhanced ascent over the precipitation domain and the strong

364   meridional TCWV anomaly gradient explain the strongly enhanced precipitation anomalies in the

365   wet surge composites. These results are consistent with the GPM precipitation anomaly and B_L

366   results.

367   *4.2 Transect analysis of cold surges*

368   ERA5 data are also averaged over 7 transects that are spaced at 0.25° along the South China

369   Sea (see the "Transect analysis region", orange box in Figure 1). Nearest-neighbour interpolation

370   is performed for each variable along each transect at the same horizontal resolution. The north-

371   easterly component of the 925 hPa along-transect wind anomalies depict a rapid acceleration of

372   negative anomalies towards the equator in cold surges from about day -2 (Figure 6a). Wind

373   anomalies peak under -5 m s^{-1} on day +1 when the surge is strongest. θ_e anomalies at 925 hPa are

374   also an indicator of both temperature and moisture anomalies (Figure 6b). Overall, negative 925

375   hPa θ_e anomalies (i.e., cold and dry anomalies; peaking at approximately -9 K), which are likely

376   associated with the Siberian high outflow, are advected much slower towards the equator

377   (approximately 5 m s^{-1}) compared to the propagation of north-easterly winds (approximately 30 m

378   s^{-1}). This finding is consistent with the Rossby adjustment problem on the beta plane by Lim and

379   Chang (1981), where the establishment of the Rossby wave group from the Siberian high explains

380   the development of the north-easterly wind flow. Chang et al. (1983) takes the theoretical

381   framework of Lim and Chang (1981) further to show that cold surges occurred in two distinct

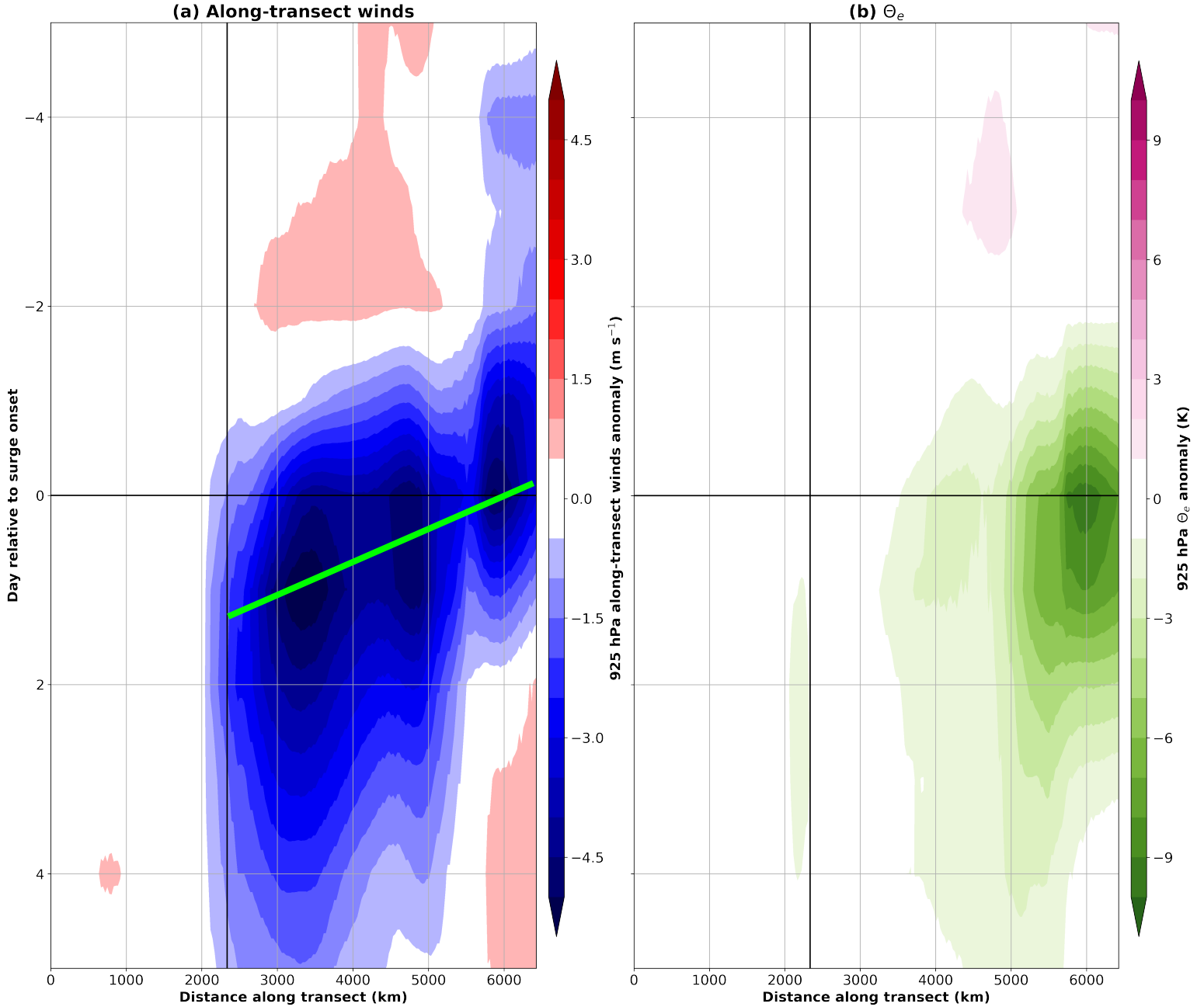382   stages. The first stage was characterised by a significant rise in surface pressure at the cold surge

Figure 6: Lagged composite plots of transect-averaged daily mean anomalies of 925 hPa (a) along-transect winds and (b) θₑ from day -5 to day +5 relative to surge onset with the seasonal cycle removed. The mean of all 545 cold surge days is taken. The transects are averaged over the orange box in Figure 1. The approximate location of the equator is marked by the vertical black line, and the transects are constructed from south-west to north-east moving left to right. Along-transect winds are negative moving north-east to south-west. The green line indicates the approximate speed of the north-easterly surge wind propagation.

383   'edge' and gravity-wave type motions associated with equatorial propagation at about 40 m s⁻¹,

384   and the second stage featured a sharp decrease in surface dew point temperature accompanied by

385   a decrease in surface temperature that were associated with a cold front passage. Following both

386   stages was a strengthening of the surface wind, often with a northerly acceleration (Chang et al.,

387   1979, 1983). Therefore, the propagation of the surge may be viewed as a transient motion under

388   the adjustment of the pressure-wind imbalance. This explains the faster propagation speed of

389   north-easterly winds relative to the slower advection velocity of negative 925 hPa θ_e anomalies in

390   our cold surge composites.

391   The vertical structure of the θ_e anomalies are then compared for the dry, wet, and moderate

392   cold surge composites from 1000 to 100 hPa (Figure 7). We include vectors for the magnitudes of

393   along-transect winds and ω to show areas of convergence and divergence, and ascent and descent,

394   respectively. ω is also exaggerated by a factor of 50. In all cases, descent and negative θ_e anomalies

395   deepen and strengthen between day -1 and day +1, strongest within the lower troposphere

396   (approximately 1000 to 750 hPa) and in the dry surge composites (under -7 K; Figures 7a, d).

397   Towards the north-eastern end of the transect, north-easterly winds also extend from the surface

398   to approximately 700 hPa before shifting to south-westerly aloft.

399   Areas of convergence and uplift at the lower levels (with divergence towards the upper

400   troposphere) correspond to positive low-level θ_e anomalies and enhanced precipitation anomalies.

401   Descent and negative θ_e anomalies are associated with negative precipitation anomalies. Cold and

402   dry anomalies are already observed on day -1 over most of the South China Sea in the dry surge

403   composites (-1 to -3 K; Figure 7a). Warm and moist anomalies are observed in the wet surge

404   composites approximately between the equator and 12°N (+1 to +2 K; Figure 7b). In both cases

405   the anomalies extend from approximately 900 to 450 hPa. On day +1 in the wet composites,

406   positive θ_e anomalies become more widespread along the South China Sea, and increase with

407   height from the surface (0 to -1 K) to approximately 800 hPa (+1 to +3 K; Figure 7e). Precipitation
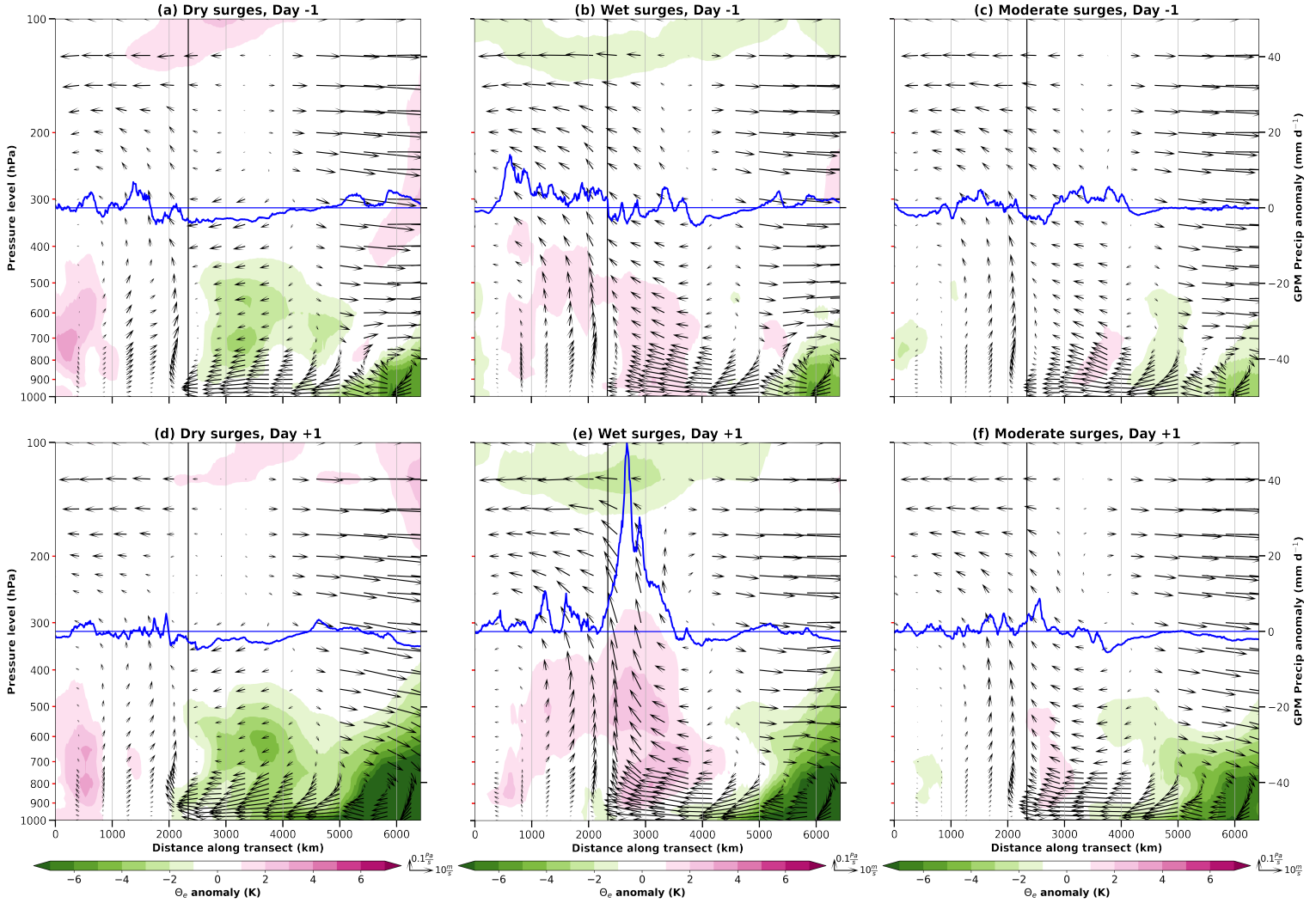
Figure 7: Lagged composite plots of transect-averaged daily mean ERA5 θ_e anomalies from 1000 to 100 hPa (contours) and daily mean GPM precipitation anomalies (blue lines) with the seasonal cycle removed. (a, d) Dry, (b, e) wet, and (c, f) moderate cold surges on day -1 (top row) and day +1 (bottom row) relative to surge onset. The wind vectors represent the magnitudes of daily mean along-transect winds and ω. ω is exaggerated by a factor of 50. The transects are averaged over the orange box in Figure 1. The approximate location of the equator is marked by the vertical black line, and the transects are constructed from south-west to north-east moving left to right.

408   anomalies are highest (peaking at approximately +45 mm d^{-1}) just to the north of the equator where

409   positive θ_e anomalies and ascent are strongest. This vertical gradient in θ_e anomalies means that

410   the lowest layers of the atmosphere are potentially stable. In the moderate surge composites (Figure

411   7c, f), both the cold and dry anomalies from the surge (up to -7 K at the northeastern end of the

412   transect), and warm and moist anomalies (0 to +1 K) near the equator follow a similar pattern to

413   that of the wet surge composites. Finally, the extent of cross-equatorial flow is greatest in the dry

414   surge composites and least in the wet surge composites, which is consistent with wind patterns in

415   Figure 5.

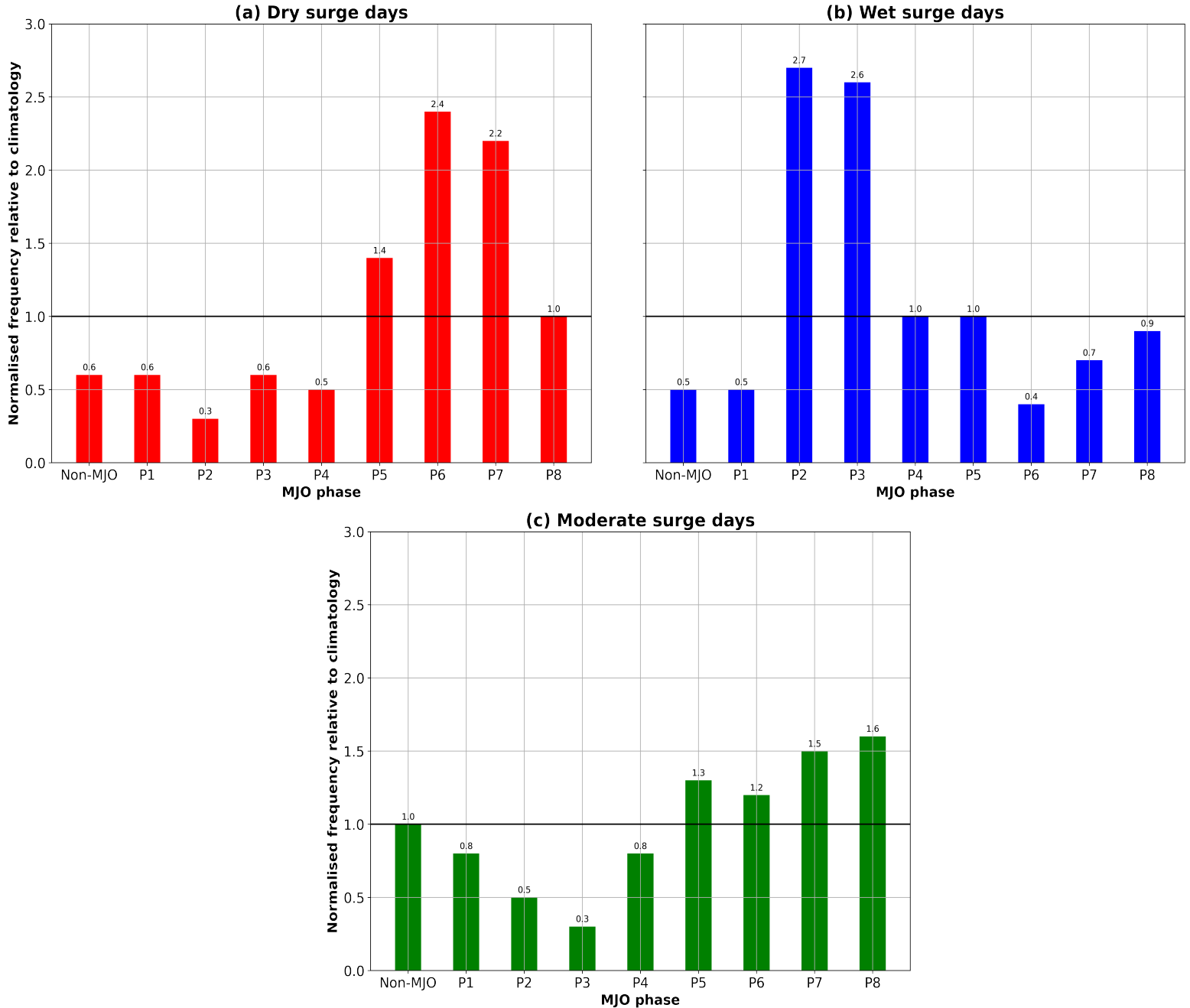416   **5 Cold surges, MJO, and Australian summer monsoon bursts**

Figure 8: Normalised frequency for phases of the MJO (including non-MJO days) relative to climatology. (a) Dry, (b) wet, and (c) moderate cold surge days. The horizontal black line is drawn at a normalised frequency of 1.0, where the percentage occurrence of a particular phase of the MJO is equal to that of climatology.

417   Figure 8 shows the normalised frequency of cold surge days in each phase of the MJO

418   (including non-MJO days) relative to climatology for the three surge categories. There is a clear

419   correlation between the phase of the MJO and the number of dry or wet surge days, although the

420   presence of a surge in each category is not uniquely tied to particular phases of the MJO. Dry surge

421   days have normalised frequencies that peak at approximately 2.4 and 2.2 in phases 6 and 7

422   respectively (Figure 8a), whereas wet surge days have peaks at approximately 2.7 and 2.6 in phases

423   2 and 3 respectively (Figure 8b). For moderate surge days (Figure 8c), the normalised frequency

424   is lowest in phase 3 (approximately 0.3) and highest in phase 8 (approximately 1.6). Here, the

425   frequency of the active phases is reduced while that of the suppressed phases is increased. In phases

426   5-8, the normalized frequencies are all greater than 1. These findings agree with the Chang et al.

427   (2005) and Lim et al. (2017) studies which reported southwesterly anomalies over a large area of

428   East Asia and western Pacific during phases 2 and 3. According to Lim et al. (2017), these

429   anomalies are consistent with the Rossby wave response to the MJO convection pattern, which

430   partially counter the north-easterly cold surge winds.

431   To better understand the influence of the MJO on cold surges, composites of daily mean

432   MSLP anomalies (Figures 9a-d) and GPM precipitation anomalies (Figures 9e-h) are shown in

433   the active phases for the wet surge composites and suppressed phases for the dry composites. The

434   non-dominant or non-MJO phases are also compared for both categories. The same analysis is

435   conducted over the Australian monsoon domain (see the green box in Figure 1; Figures 15 and

436   16). Based on Figure 8, phases 5-7 are composited for the dry surges and phases 2-3 for the wet

437   surges. Another set of composites are taken for all other phases of the MJO and non-MJO days to

438   expose the effect of removing the dominant MJO signal. In all cases, the north-easterly wind

439   anomalies from the cold surge are consistently associated with positive MSLP anomalies, which

440   are strongest at the northernmost part of the region over inland Southern China (peaking over +5.0

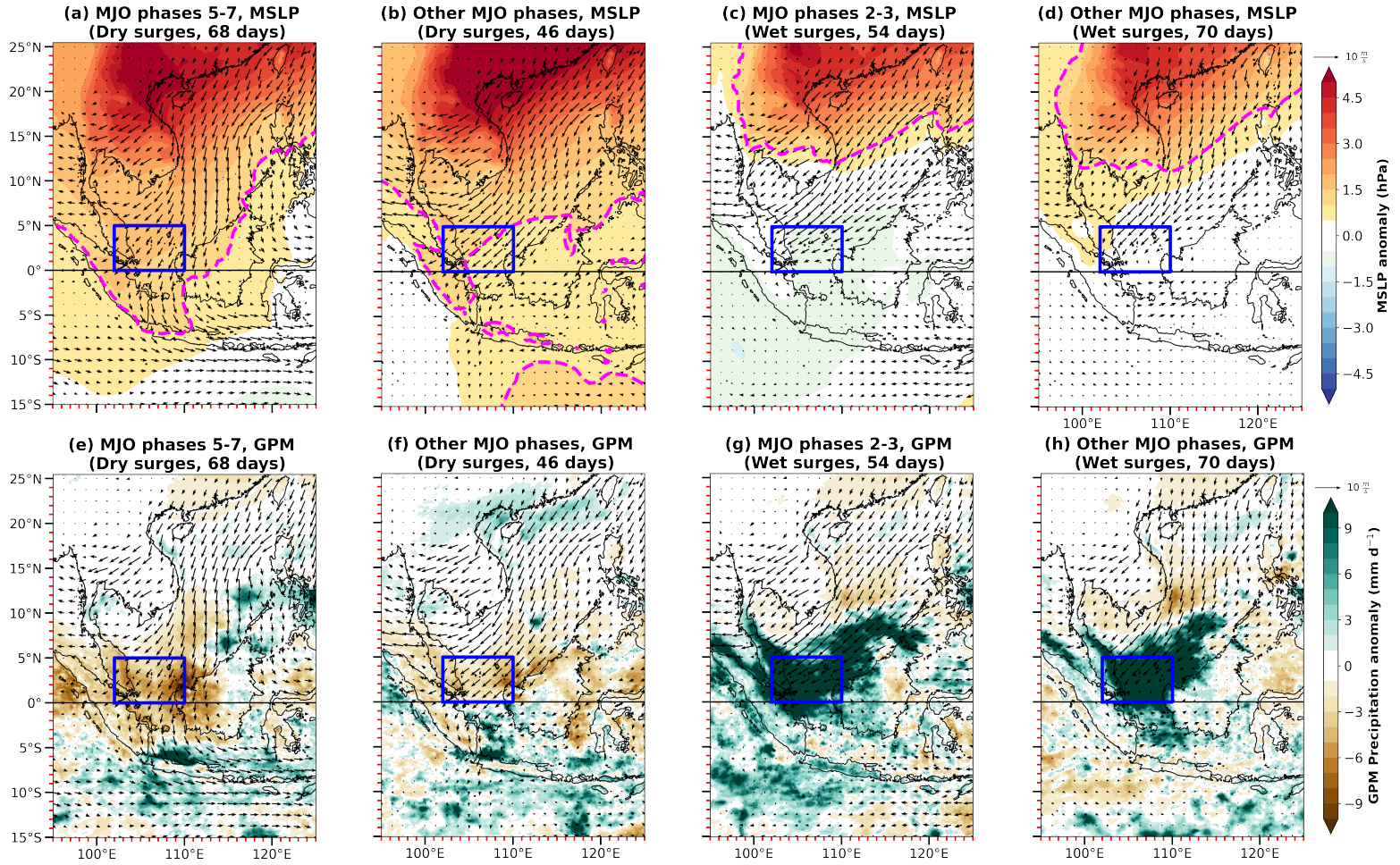441   hPa in the dry surge composites).

Figure 9: Composite maps of daily mean (a-d) MSLP anomalies and (e-h) GPM precipitation anomalies (bottom) with the seasonal cycle removed. Daily mean 925 hPa horizontal wind anomaly vectors. Dry and wet cold surges in both the dominant phases of the MJO (a, c, e, g), and all other phases including non-MJO days (b, d, f, h). The precipitation domain is depicted by the blue box. The dashed pink line on the MSLP plots represents the +1.0 hPa MSLP anomaly.

442   In the dry surge composites, the +1.0 hPa MSLP anomalies cross the equator and extend

443   to Java, as with the cross-equatorial wind flow. These circulation patterns are characteristic of the

444   'Both type' surges in Abdillah et al. (2021). Westerly anomalies are widespread over Java in

445   phases 5-7 of the MJO along with weak low-pressure anomalies to the south-east of the domain (-

446   0.5 hPa; Figure 9a). Widespread high-pressure anomalies are observed outside these suppressed

447   phases of the MJO, with no westerly anomalies over Java (Figure 9b). In both cases, an inverse

448   relationship in rainfall is found with negative precipitation anomalies (peaking close to -10 mm d^{-1}

449   in the suppressed phases of the MJO) over the precipitation domain and strongly enhanced

450   precipitation anomalies (peaking over +10 mm d^{-1}) off the north-west coast of Java. The

451   precipitation gradients are stronger in the suppressed phases of the MJO. On the other hand, the

452   +1.0 hPa contour in the wet surge composites is confined to above 10°N, which is characteristic

453   of the 'South China Sea type' surge in Abdillah et al. (2021). Positive MSLP anomalies extend

454   further equatorward outside the active phases of the MJO (Figure 9d). In contrast, the active phases

455   coincide with weak low pressure anomalies (-0.5 to -1.0 hPa) over most of the precipitation

456   domain, Java, and the Indian Ocean (Figure 9c). In both cases, a cyclonic circulation is evident

457   around Borneo, which corresponds to the large area of strongly enhanced precipitation anomalies

458   over the equatorial South China Sea. There are also patches of dry anomalies (-1 to -7 mm d^{-1})

459   further north along the South China Sea and no strongly enhanced precipitation anomalies over

460   the Java region unlike the dry surge composites.

461   Over the Australian monsoon domain, the widespread westerly anomalies in phases 5-7 of

462   the MJO for the dry surge composites are associated with a strong north-west to south-east pressure

463   gradient between Java and northern Australia (Figure 10a). Low pressure anomalies just off the

464   north-west coast of northern Australia and at the southern end of the domain peak just under -1.0

465   hPa. In contrast, the wet surge composites in phases 2-3 of the MJO depict a reversed pressure

466   gradient associated with easterly anomalies, with widespread high pressure anomalies exceeding

467   +1.0 hPa over much of northern Australia (Figure 10c). According to Wheeler and Hendon (2004),

468   phases 5-7 (phases 2-3) are the active (suppressed) phases of the MJO over the northern Australian

469   region. Outside these dominant phases, there are widespread high pressure anomalies in the dry

470   surge composites exceeding +1.0 hPa over most of the domain associated with weak easterly

471 anomalies (Figure 10b). On the other hand, low pressure anomalies (-0.1 to -0.9 hPa) and relatively

472 weak westerly anomalies are found over most of northern Australia in the wet surge composites
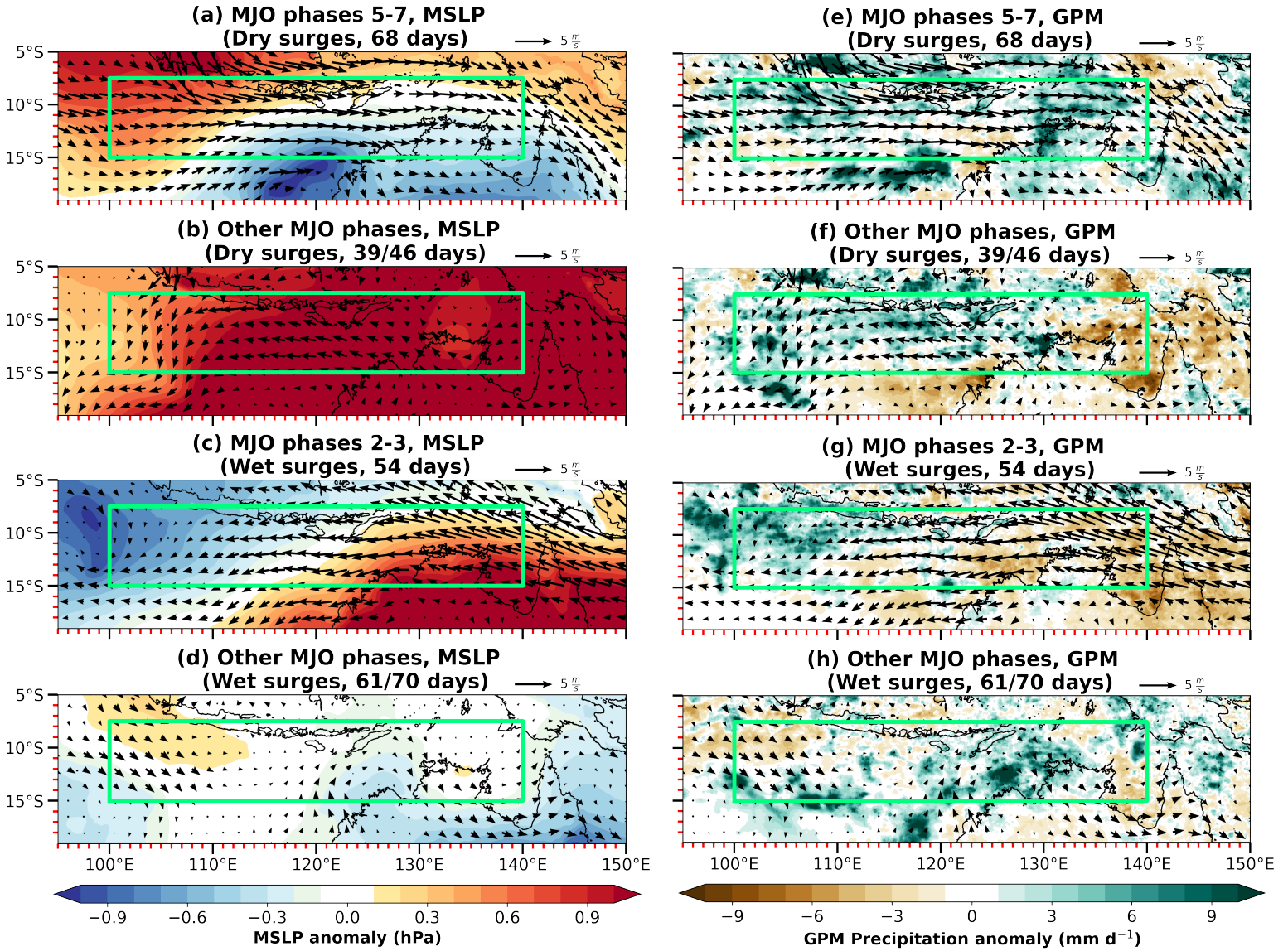
473 (Figure 10d).

Figure 10: Composite maps of daily mean (a-d) MSLP anomalies and (e-h) GPM precipitation anomalies with the seasonal cycle removed. Daily mean 925 hPa horizontal wind anomaly vectors. Dry and wet cold surges in both the dominant phases of the MJO (a, c, e, g), and all other phases including non-MJO days (b, d, f, h). The Australian monsoon domain is depicted by the green box. Cold surges that coincide with strong tropical cyclones over northern Australia within the non-dominant/non-MJO phases are removed.

474 GPM rainfall patterns over the Australian monsoon domain are also largely influenced by

475 the MJO patterns. Strongly enhanced precipitation anomalies (exceeding +10 mm d^{-1} in some

476   areas) are most widespread during the active phases of the MJO (Figure 10e) while dry anomalies

477   are found over much of northern Australia in the suppressed phases (-1 to -7 mm d^{-1}; Figure 10g).

478   Outside the dominant phases, negative precipitation anomalies are found over much of northern

479   Australia in the dry surge composites (Figure 10f; peaking close to -10 mm d^{-1}), whereas patches

480   of strongly enhanced precipitation anomalies are found in the wet surge composites (Figure 10h).

481   The strongly enhanced precipitation anomalies here appear to be less connected to monsoon bursts

482   compared to the dry surge composites in phases 5-7 of the MJO since the westerly anomalies are

483   relatively weak.

484   From vertical profiles of zonal winds (Figure 11a), westerlies peak around 900 hPa in all

485   cases, but are strongest (close to 5 m s^{-1}) in the dry surge composites and weakest in the non-surge

486   composites. In the dry and moderate surge composites, the westerlies extend to approximately 450

487   hPa, which is close to the 'deep westerly regime' profile in Pope et al. (2009), who investigated

488   the regimes of the wet season in northern Australia. In their study, westerlies reach 350 hPa before

489   transitioning to easterlies. On the other hand, the wet surge and non-surge composites depict only

490   shallow westerlies, from the surface to approximately 800 hPa, and their zonal wind profiles are

491   similar. Meridional winds (Figure 11b) are generally weak (<1 m s^{-1}) in all composites throughout

492   most of the troposphere, although northerly winds (peaking close to -0.5 m s^{-1}) are found from

493   1000 to 900 hPa in the dry surge composites, which are likely a result of cross-equatorial
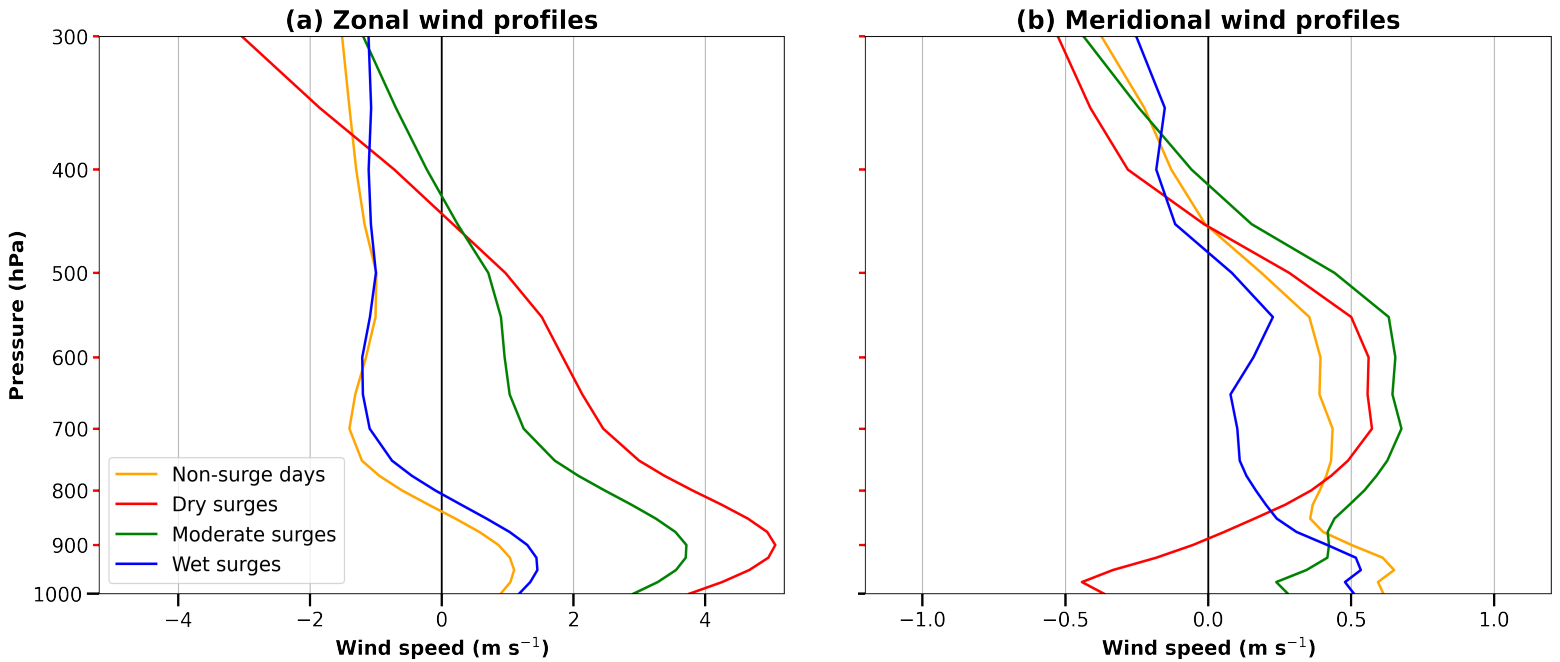
494   from cold surges.

Figure 11: Vertical profiles of (a) zonal and (b) meridional winds from 1000 to 300 hPa averaged over the Australian monsoon domain. Non-surge days (orange), and dry (red), moderate (green), and wet (blue) cold surge composites.

495   From these results, the MJO appears to be the primary influence of the cross-equatorial

496   flow from cold surges, westerlies, and Australian summer monsoon bursts. This is also consistent

497   with the finding that most dry (wet) surges according to the precipitation domain coincide with

498   phases 5-7 (phases 2-3) of the MJO. The MJO influence also explains why the majority of cases

499   within the dry surge composites would be associated with westerlies and bursts in the Australian

500   summer monsoon and vice versa in the wet surge composites. Cross-equatorial surges can also be

501   thought of as the westerly part of the MJO. While the influences of cross-equatorial flow from cold

502   surges and the effects of the MJO cannot be separated, the westerlies over Australia are better

503   explained as part of MJO circulations rather than cold surges. The MJO influence over the

504   Australian summer monsoon is also consistent with findings from Berry and Reeder (2016) and

505   Narsey et al. (2017).

6 Conclusions

In this study, we analysed the synoptic structure and development of dry, moderate, and wet cold surges over the Maritime Continent region over 20 November-March seasons. The study included an investigation of both the seasonal and diurnal cycles. We also examined the relationship between the MJO and cold surges and bursts in the Australian summer monsoon.

The plume buoyancy, introduced by Adames et al. (2021), was used to better understand the convection associated with cold surges, and to delineate the three categories studied. In the 20-year climatology, there is an exponential increase in precipitation as B_L increases towards zero, as found by Adames et al. (2021). Most wet surge days exceed the -0.02 m s^{-2} threshold for B_L and vice versa for most dry surge days. The diurnal cycle of B_L is also consistent with that of GPM precipitation anomalies, and is suppressed over the precipitation domain. Strongly enhanced wet anomalies are found over much of the precipitation domain and equatorial South China Sea in the wet surges throughout the day, especially during the nocturnal hours. Our findings imply that the wet surges are characterised by a moister free troposphere that allows convection to penetrate through the lower troposphere.

In terms of synoptic environments, cold surges over the northern South China Sea are generally characterised by negative TCWV anomalies, and enhanced descent from negative 700 hPa ω anomalies. For the dry surge composites, enhanced descent or weaker ascent and dry air reach the precipitation domain, and enhanced ascent and moist air over Java. In the wet surge composites, the meridional TCWV anomaly gradient is located further to the north where the anomalies are positive over the precipitation domain. Here, the moist anomalies prior to surge onset are also consistent with our plume buoyancy results. The large areas of strongly enhanced ascent is also consistent with GPM precipitation anomaly patterns.

529   There is also a rapid acceleration of north-easterly wind anomalies towards the equator

530   associated with the cold surge, but negative θ_{e925} anomalies associated with the Siberian high

531   outflow are advected more slowly. Here, the propagation of the surge may be viewed as a transient

532   motion under the adjustment of the pressure-wind imbalance. In the vertical, descent with cold

533   and dry anomalies deepen and strengthen between day -1 and day +1, and are strongest and most

534   widespread in the dry surge composites. Warm and moist anomalies are most widespread near the

535   equator on day +1 in the wet surge composites, and the vertical gradient in θ_e anomalies means

536   that the lowest layers of the atmosphere are potentially stable. The corresponding precipitation

537   anomalies just to the north of the equator peak at approximately +45 mm d^{-1}.

538   Most of the dry surges occur during the suppressed phases of the MJO (phases 5-7) while

539   most of the wet surges occur during the active phases (phases 2-3). When the suppressed phases

540   of the MJO are over the precipitation domain in the dry surge composites, westerly anomalies

541   coincide with high-pressure anomalies over Java and low-pressure anomalies over northern

542   Australia. Here, the influence of cross-equatorial surges and the MJO on westerlies and the bursts

543   in the Australian summer monsoon is clearest, which is also evident from the areas of strongly

544   enhanced precipitation anomalies in these regions. The lack of cross-equatorial flow and westerlies

545   outside phases 5-7 coincide with widespread high-pressure anomalies extending to Java and

546   northern Australia. In the wet surge composites, weak low-pressure anomalies are observed over

547   much of the equatorial region during the active phases. The cyclonic circulation near Borneo in

548   the wet surge composites coincides with the large area of strongly enhanced precipitation

549   anomalies over the equatorial South China Sea, and a lack of cross-equatorial flow compared to

550   the dry surge composites. Over northern Australia, strong high-pressure anomalies are found with

551   low pressure anomalies over Java in MJO phases 2-3, which is opposite to the MSLP gradient in

552   phases 5-7 for the dry composites. Overall, the MJO appears to be the primary influence in

553   producing cross-equatorial flow, and the associated precipitation and westerlies in the Australian

554   summer monsoon.

555   Finally, deep westerlies are evident over the northern Australia domain in both the dry and

556   moderate surge composites, while shallow westerlies are found in the wet surge composites and

557   climatology. Northerly winds are also found between 1000 and 900 hPa in the dry surge

558   composites, which are likely a result of cross-equatorial flow associated with an active phase of

559   the MJO (phases 5-7 over northern Australia).

570   **Open Research**

571   Data Availability Statement

572   All data used in this manuscript are publicly available. The ERA5 dataset is publicly available at

573   https://www.ecmwf.int/en/forecasts/datasets/reanalysis-datasets/era5,   and   the   National

574   Computational Infrastructure (NCI) supercomputer (https://nci.org.au/) was remotely accessed to

575 analyse the ERA5 datasets from the rt52 workspace. The NASA GPM data may be obtained from

576 https://doi.org/10.5067/GPM/IMERGDF/DAY/06 for daily data and

577 https://doi.org/10.5067/GPM/IMERG/3B-HH/06 for half-hourly data. Daily MJO data are

578 available from the Australian Bureau of Meteorology at http://www.bom.gov.au/climate/mjo/.

579 **References**

580 Abdillah, M. R., Kanno, Y., Iwasaki, T., & Matsumoto, J. (2021). Cold Surge Pathways in East

581 Asia and Their Tropical Impacts. *Journal of Climate, 34*(1), 157-170.

582 https://journals.ametsoc.org/view/journals/clim/34/1/jcliD200552.xml

583

584 Adames, Á. F., Powell, S. W., Ahmed, F., Mayta, V. C., & Neelin, J.D. (2021). Tropical

585 Precipitation Evolution in a Buoyancy-Budget Framework, *Journal of the Atmospheric Sciences,*

586 *78*(2), 509-528. https://doi.org/10.1175/JAS-D-20-0074.1

587

588 Ahmed, F., & Neelin, J. D. (2018). Reverse Engineering the Tropical Precipitation–Buoyancy

589 Relationship. *Journal of the Atmospheric Sciences, 75*(5), 1587-1608.

590 https://journals.ametsoc.org/view/journals/atsc/75/5/jas-d-17-0333.1.xml

591

592 Argüeso, D., Romero, R., & Homar, V. (2020). Precipitation Features of the Maritime Continent

593 in Parameterized and Explicit Convection Models. *Journal of Climate, 33*(6), 2449-2466.

594 https://doi.org/10.1175/JCLI-D-19-0416.1

595

596 Berry, G. J., & Reeder, M. J. (2016). The Dynamics of Australian Monsoon Bursts. *Journal of the*

597 *Atmospheric Sciences, 73*(1), 55-69. https://doi.org/10.1175/JAS-D-15-0071.1

598

599   Chang, C.-P., Erickson, J. E., & Lau, K. M. (1979). Northeasterly Cold Surges and Near-Equatorial

600   Disturbances over the Winter MONEX Area during December 1974. Part I: Synoptic Aspects.

601   *Monthly   Weather   Review,   107*(7),   812-829.   https://doi.org/10.1175/1520-

602   0493(1979)107<0812:NCSANE>2.0.CO;2

603

604   Chang, C.-P., Harr, P. A., & Chen, H.-J. (2005). Synoptic Disturbances over the Equatorial South

605   China Sea and Western Maritime Continent during Boreal Winter. *Monthly Weather Review,*

606   *133*(3), 489-503. https://doi.org/10.1175/MWR-2868.1

607

608   Chang, C.-P., Liu, C.-H., & Kuo, H.-C. (2003). Typhoon Vamei: An equatorial tropical cyclone

609   formation. *Geophysical Research Letters, 30*(3).

610   https://agupubs.onlinelibrary.wiley.com/doi/abs/10.1029/2002GL016365

611

612   Chang, C.-P., Lu, M.-M., & Wang, S. (2004). THE EAST ASIAN WINTER MONSOON. In *The*

613   *Global Monsoon System* (pp. 99-109).

614

615   Chang, C.-P., Millard, J. E., & Chen, G. T. J. (1983). Gravitational Character of Cold Surges during

616   Winter MONEX. *Monthly Weather Review, 111*(2), 293-307. https://doi.org/10.1175/1520-

617   0493(1983)111<0293:GCOCSD>2.0.CO;2

618

619   Davidson, N. E., McBride, J. L., & McAvaney, B. J. (1983). The Onset of the Australian Monsoon

620   During Winter MONEX: Synoptic Aspects. *Monthly Weather Review, 111*(3), 496-516.

621   https://doi.org/10.1175/1520-0493(1983)111<0496:TOOTAM>2.0.CO;2

622

623   de Rooy, W. C., & Siebesma, A. P. (2010). Analytical expressions for entrainment and detrainment

624   in cumulus convection. *Quarterly Journal of the Royal Meteorological Society, 136*(650), 1216-

625   1227. https://rmets.onlinelibrary.wiley.com/doi/abs/10.1002/qj.640

626

627   Ding, Y.H. (1994). *Monsoons over China*. Boston: Kluwer Academic Publishers, 91-173.

628

629   Fong, M. and Ng, L.K. (2012). *The weather and climate of Singapore*. Singapore: Meteorological

630   Service Singapore, 70-97.

631

632   Gregory, D. (2001). Estimation of entrainment rate in simple models of convective clouds.

633   *Quarterly   Journal   of   the   Royal   Meteorological   Society,   127*(571),   53-72.

634   https://rmets.onlinelibrary.wiley.com/doi/abs/10.1002/qj.49712757104

635

636   Hersbach, H., Bell, B., Berrisford, P., Hirahara, S., Horányi, A., Muñoz-Sabater, J., et al. (2020).

637   The ERA5 global reanalysis. *Quarterly Journal of the Royal Meteorological Society, 146*(730),

638   1999-2049. https://rmets.onlinelibrary.wiley.com/doi/abs/10.1002/qj.3803

639

640   Huffman, G. J., Bolvin, D. T., Braithwaite, D., Hsu, K., Joyce, R., Kidd, C., Nelkin, E. J.,

641   Sorooshian, S., Tan, J., & Xie, P. (2019). NASA Global Precipitation Measurement (GPM)

642   Integrated Multi-satellitE Retrievals for GPM (IMERG), Algorithm Theoretical Basis Document

643   (ATBD) Version 06. *National Aeronautics and Space Administration*.

644

645 Johnson, R. H., & Chang, C.-P. (2007). WINTER MONEX: A Quarter-Century and Beyond.

646 *Bulletin of the American Meteorological Society, 88*(3), 385-388. www.jstor.org/stable/26217263

647

648 Johnson, R. H., & Houze, R. A., Jr. (1987). Precipitating cloud systems of the Asian monsoon.

649 *Monsoon Meteorology*. https://ci.nii.ac.jp/naid/10014597164/en/

650

651 Lau, K.-M., & Li, M.-T. (1984). The Monsoon of East Asia and its Global Associations—A

652 Survey. *Bulletin of the American Meteorological Society, 65*(2), 114-125.

653 https://doi.org/10.1175/1520-0477(1984)065<0114:TMOEAA>2.0.CO;2

654

655 Lim, H., & Chang, C.-P. (1981). A Theory for Midlatitude Forcing of Tropical Motions during

656 Winter Monsoons. *Journal of the Atmospheric Sciences, 38*(11), 2377-2392.

657 https://doi.org/10.1175/1520-0469(1981)038<2377:ATFMFO>2.0.CO;2

658

659 Lim, S. Y., Marzin, C., Xavier, P., Chang, C.-P., & Timbal, B. (2017). Impacts of Boreal Winter

660 Monsoon Cold Surges and the Interaction with MJO on Southeast Asia Rainfall. *Journal of*

661 *Climate, 30*(11), 4267-4281. https://doi.org/10.1175/JCLI-D-16-0546.1

662

663 Love, G. (1985). Cross-Equatorial Influence of Winter Hemisphere Subtropical Cold Surges.

664 *Monthly Weather Review, 113*(9), 1487-1498. https://doi.org/10.1175/1520-

665 0493(1985)113<1487:CEIOWH>2.0.CO;2

666

667 Meteorological Service Singapore [MSS]. (2022). *Weather Systems*. Retrieved 8 August, 2022,

668 from http://www.weather.gov.sg/learn_weather_systems/

669

670 Meteorological Service Singapore [MSS]. (2022a). *2021 Annual Climate Assessment Singapore.*

671 Retrieved 8 August 2022, from http://www.weather.gov.sg/climate-annual-climate-reports/

672

673 Narsey, S., Reeder, M. J., Ackerley, D., & Jakob, C. (2017). A Midlatitude Influence on Australian

674 Monsoon Bursts. *Journal of Climate, 30*(14), 5377-5393. https://doi.org/10.1175/JCLI-D-16-

675 0686.1

676

677 Narsey, S., Reeder, M. J., Jakob, C., & Ackerley, D. (2018). An Evaluation of Northern Australian

678 Wet Season Rainfall Bursts in CMIP5 Models. *Journal of Climate, 31*(19), 7789-7802.

679 https://doi.org/10.1175/JCLI-D-17-0637.1

680

681 National Aeronautics and Space Administration [NASA]. (2021). *Global Precipitation*

682 *Measurement*. Retrieved 4 February, 2021, from https://gpm.nasa.gov/data-

683 access/downloads/gpm

684

685 Neale, R., & Slingo, J. (2003). The Maritime Continent and Its Role in the Global Climate: A

686 GCM Study. *Journal of Climate, 16*(5), 834-848. https://doi.org/10.1175/1520-

687 0442(2003)016<0834:TMCAIR>2.0.CO;2

688

689 Pope, M., Jakob, C., & Reeder, M. J. (2009). Regimes of the North Australian Wet Season.

690 *Journal of Climate, 22*(24), 6699-6715.

691 https://journals.ametsoc.org/view/journals/clim/22/24/2009jcli3057.1.xml

692

693   Pullen, J., Gordon, A. L., Flatau, M., Doyle, J. D., Villanoy, C., & Cabrera, O. (2015). Multiscale

694   influences on extreme winter rainfall in the Philippines. *Journal of Geophysical Research:*

695   *Atmospheres, 120*(8), 3292-3309.

696   https://agupubs.onlinelibrary.wiley.com/doi/abs/10.1002/2014JD022645

697

698   Ramage, C. S. (1968). ROLE OF A TROPICAL "MARITIME CONTINENT" IN THE

699   ATMOSPHERIC CIRCULATION1. *Monthly Weather Review, 96*(6), 365-370.

700   https://doi.org/10.1175/1520-0493(1968)096<0365:ROATMC>2.0.CO;2

701   Ramage, C.S. (1971). *Monsoon Meteorology*. London: Academic Press, 229-242.

702

703   Raymond, D., Fuchs, Ž., Gjorgjievska, S., & Sessions, S. (2015). Balanced dynamics and

704   convection in the tropical troposphere. *Journal of Advances in Modeling Earth Systems, 7*(3),

705   1093-1116. https://agupubs.onlinelibrary.wiley.com/doi/abs/10.1002/2015MS000467

706

707   Suppiah, R., & Wu, X. (1998). Surges, cross-equatorial flows and their links with the Australian

708   summer monsoon circulation and rainfall. *Australian Meteorological Magazine, 47*(2), 113-130.

709

710   Tangang, F. T., Juneng, L., Salimun, E., Vinayachandran, P. N., Seng, Y. K., Reason, C. J. C., et

711   al. (2008). On the roles of the northeast cold surge, the Borneo vortex, the Madden-Julian

712   Oscillation, and the Indian Ocean Dipole during the extreme 2006/2007 flood in southern

713   Peninsular Malaysia. *Geophysical Research Letters, 35*(14).

714   https://agupubs.onlinelibrary.wiley.com/doi/abs/10.1029/2008GL033429

715

716   Wheeler, M. C., & Hendon, H. H. (2004). An All-Season Real-Time Multivariate MJO Index:

717   Development of an Index for Monitoring and Prediction. *Monthly Weather Review, 132*(8),

718   1917-1932. https://journals.ametsoc.org/doi/abs/10.1175/1520-

719   0493%282004%29132%3C1917%3AAARMMI%3E2.0.CO%3B2

720

721   Wu, P., Hara, M., Fudeyasu, H., Yamanaka, M. D., Matsumoto, J., Syamsudin, F., et al. (2007).

722   The Impact of Trans-equatorial Monsoon Flow on the Formation of Repeated Torrential Rains

723   over Java Island. *SOLA, 3*, 93-96. https://doi.org/10.2151/sola.2007-024

724

725   Xavier, P., Lim, S. Y., Ammar Bin Abdullah, M. F., Bala, M., Chenoli, S. N., Handayani, A. S.,

726   et al. (2020). Seasonal Dependence of Cold Surges and their Interaction with the Madden–Julian

727   Oscillation   over   Southeast   Asia.   *Journal   of   Climate,   33*(6),   2467-2482.

728   https://doi.org/10.1175/JCLI-D-19-0048.1

729

730   Yang, J.H., Qian, J.H., & Timbal, B. (2019). A moisture flux perspective on cold surges and wet

731   spells affecting Singapore. *MSS Research Letters*. Issue 3, 3-9. Retrieved 4 February, 2021, from

732   http://ccrs.weather.gov.sg/wp-content/uploads/2019/07/MRL_Issue_3_Jul2019_FINAL.pdf

733   \Yihui, D. (1990). Build-up, air mass transformation and propagation of Siberian high and its

734   relations to cold surge in East Asia. *Meteorology and Atmospheric Physics, 44*(1), 281-292.

735   https://doi.org/10.1007/BF01026822

736

737   Yihui, D. (1994). *Monsoons over China*. Boston: Kluwer Academic Publishers, 91-173.

738 **FIGURE CAPTION GUIDE**

739 **Figure 1**. The figure caption should begin with an overall descriptive statement of the figure followed by additional

740 text. They should be immediately after each figure. Figure parts are indicated with lower-case letters (**a, b, c…**). For

741 initial submission, please place both the figures and captions in the text near where they are cited rather than at the

742 end of the file (not both). At revision, captions can be placed in-text or at the end of the file, and figures should be

743 uploaded separately. Each figure should be one complete, cohesive file (please do not upload sub-figures or figure

744 parts in separate files.